Many-body theory of positron-atom interactions

G. F. Gribakin* and J. Ludlow†

Department of Applied Mathematics and Theoretical Physics, Queen's University, Belfast BT7 1NN, Northern Ireland, United Kingdom
(Received 23 March 2004; published 29 September 2004)

A many-body theory approach is developed for the problem of positron-atom scattering and annihilation. Strong electron-positron correlations are included nonperturbatively through the calculation of the electron-positron vertex function. It corresponds to the sum of an infinite series of ladder diagrams, and describes the physical effect of virtual positronium formation. The vertex function is used to calculate the positron-atom correlation potential and nonlocal corrections to the electron-positron annihilation vertex. Numerically, we make use of *B*-spline basis sets, which ensures rapid convergence of the sums over intermediate states. We have also devised an extrapolation procedure that allows one to achieve convergence with respect to the number of intermediate-state orbital angular momenta included in the calculations. As a test, the present formalism is applied to positron scattering and annihilation on hydrogen, where it is exact. Our results agree with those of accurate variational calculations. We also examine in detail the properties of the large correlation corrections to the annihilation vertex.

I. INTRODUCTION

The interaction of a low-energy positron with a many-electron atom is characterized by strong correlation effects. Apart from the dynamic polarization of the electron cloud by the field of the positron, the positron can also form positronium (Ps), by picking up one of the atomic electrons. When the positron energy is below the Ps-formation threshold, $\varepsilon_{Ps} = I + E_{1s}(Ps) = I - 6.8$ eV, where I is the atomic ionization potential, positronium formation is a virtual process. Nevertheless, its role in the positron-atom interaction is very important [1–4]. The main aim of this work is to develop a many-body theory approach which accounts accurately for both correlation effects, and to test it for positron scattering and annihilation on hydrogen.

The study of positron interaction with matter is a topic of fundamental interest [5]. Positrons have also found many useful applications. They are a very sensitive probe of the presence of defects in materials [6]. The recent development of a scanning positron microscope [7] may lead to an increased use of positrons for quality control of materials, particularly in the semiconductor industry. In medicine, positron emission tomography, or PET, has become a standard means of medical imaging (see, e.g., Ref. [8]). A proper understanding of how positrons interact with matter at the fundamental level of atoms and molecules is therefore essential.

The interaction of low-energy positrons with atoms has presented a challenge to the theorist for many decades. The study of positron scattering from atoms was initially seen as a useful complement to work on electron scattering, particularly in helping to understand the role of the exchange interaction. However, although the exchange interaction is absent, it was quickly realized that the positron-atom problem is more complex than the electron case. The attractive induced polarization potential tends to cancel and even overcome the static repulsion of the positron by the atom at low energies. The positron may also temporarily capture one of the atomic electrons in a process known as virtual positronium formation. The need to account for these effects requires an elaborate and accurate theoretical description.

For small systems, such as hydrogen and helium, accurate results were obtained through the use of variational methods [9–14]. Positron scattering from alkali atoms which have a single valence electron has been calculated extensively using a coupled-channel method with pseudostates [15]. More recently, positron and Ps interaction with atoms with few active (valence) electrons has been studied using the stochastic variational method (SVM) and configuration-interaction-type approaches [16–20]. However, it is difficult to extend these methods to larger atomic systems with many valence electrons, e.g., the noble gases.

An attractive alternative to few-body methods is many-body theory [21]. It lends itself naturally to the study of problems where an extra particle interacts with a closed-shell target. The use of diagrams makes this method both descriptive and intuitive, and allows one to take many-particle correlations into account in a systematic way. Many-body theory has been successful in the study of photoionization [22,23] and in problems involving electrons, such as electron-atom scattering [24–28], negative ions [29–32], and precise calculations of energies and transition amplitudes in heavy atoms with a single valence electron [33,34]. The application of many-body theory to low-energy positron interactions with atoms has met with more difficulty.

Many-body theory utilizes techniques originating in quantum field theory. It describes the terms of the perturbation series in the interaction between particles diagrammatically. The difficulty in applying this approach to the interaction of positrons with atoms arises from the need to take into account (virtual) Ps formation. Being a bound state, Ps cannot be described by a finite number of perturbation-theory terms.

─────────

*Email address: g.gribakin@am.qub.ac.uk
†Present address: Department of Physics, Auburn University, Auburn, AL 36849, USA. Email address: j.ludlow@am.qub.ac.uk

70 032720-1

Hence an infinite sequence of the "ladder" diagrams must be summed.

The first attempt to apply many-body theory to the positron-atom problem was by Amusia *et al.* in 1976 [2], who used a crude approximate method of accounting for virtual Ps formation in He. A better approximation for the virtual Ps-formation contribution was devised in Ref. [4], and applications to various atomic targets, including noble gases, were reported [35–37]. In particular, a reasonable description was obtained for positron scattering from noble-gas atoms, which highlighted the presence of positron-atom virtual levels in Ar, Kr, and Xe. On the other hand, application of the same approximation to positron-atom annihilation showed that it was clearly deficient.

In spite of the approximate treatment of virtual Ps formation, many-body theory calculations for Mg, Cd, Zn, and Hg were the first to provide credible evidence that positrons can bind to neutral atoms [35]. Two years later positron-atom binding was proved in a stochastic variational calculation for Li [38]. At present the list of atoms capable of binding positrons has expanded dramatically, SVM and configuration-interaction calculations confirming positron binding to Mg, Cd, and Zn [39,40]. This topic is now of major interest in positron physics (see Refs. [40,41] for useful reviews).

In this paper, new techniques will be outlined that allow the exact calculation of the electron-positron ladder diagram sequence which accounts for virtual Ps formation. This approach enables many-body theory to provide accurate information on the elastic scattering, annihilation, and binding of positrons on atoms and negative ions at energies below the Ps formation threshold.

II. MANY-BODY THEORY METHOD

A. Dyson equation

A conventional treatment of positron scattering from an N-electron target would start from the Schrödinger equation for the total wave function for the $N+1$ particles. In many-body theory we start instead from the Dyson equation (see, e.g., Refs. [21,42]),

$$(H_0 + \Sigma_\varepsilon)\psi_\varepsilon = \varepsilon\psi_\varepsilon, \tag{1}$$

where ψ_ε is the single-particle (quasiparticle) wave function of the positron, ε is its energy, and H_0 is a central-field Hamiltonian of the zeroth approximation, which describes the motion of the positron in the static field of the target. The many-body dynamics in Eq. (1) is represented by Σ_ε, a nonlocal energy-dependent correlation potential. This quantity, also known as the optical potential, is equal to the self-energy part of the single-particle Green's function of the positron in the presence of the atom [43]. Due to its nonlocal nature Σ_ε operates on the quasiparticle wave function as an integral operator,

$$\Sigma_\varepsilon\psi_\varepsilon = \int \Sigma_\varepsilon(\mathbf{r},\mathbf{r}')\psi_\varepsilon(\mathbf{r}')d\mathbf{r}'. \tag{2}$$

For hydrogen H_0 may simply be taken as the Hamiltonian of the positron moving in the electrostatic field of the ground-state atom, $H_0 = -\frac{1}{2}\nabla^2 + U(r)$, where $U(r) = (1 + r^{-1})e^{-2r}$ [44] (we use atomic units throughout). For systems containing more than one electron the Hartree-Fock (HF) Hamiltonian (without exchange, for the positron) is the best choice. The correlation potential Σ_ε is given by an infinite perturbation series in powers of the residual electron-electron and electron-positron interaction. Inclusion of the electrostatic interaction in H_0 and the use of the HF approximation for the target electrons means that the perturbation-theory expansion for Σ_ε starts with the second-order diagrams, and that the diagrams do not contain elements which describe the electrostatic potential [45].

Owing to the spherical symmetry of the problem, Eq. (1) can be solved separately for each positron partial wave. So, in practice one deals with radial quasiparticle wave functions, $\widetilde{P}_{\varepsilon l}(r)$, related to ψ_ε by $\psi_\varepsilon(\mathbf{r}) = r^{-1}\widetilde{P}_{\varepsilon l}(r)Y_{lm}(\Omega)$, where $Y_{lm}(\Omega)$ is the spherical harmonic for the orbital angular momentum l. Accordingly, the self-energy operator is also found for each partial wave separately, as $\Sigma_\varepsilon^{(l)}(r,r')$, see Eq. (A1) in the Appendix.

B. Correlation potential

Figure 1 shows the lowest-order terms of the diagrammatic expansion for the correlation potential Σ, or more precisely, for the matrix element $\langle\varepsilon'|\Sigma_E|\varepsilon\rangle$ of the correlation potential calculated at some energy E between the positron states ε and ε'. The leading second-order diagram, Fig. 1(a), corresponds to the following expression:

$$\langle\varepsilon'|\Sigma_E^{(2)}|\varepsilon\rangle = \sum_{\nu,\mu,n} \frac{\langle\varepsilon'n|V|\mu\nu\rangle\langle\nu\mu|V|n\varepsilon\rangle}{E - \varepsilon_\nu - \varepsilon_\mu + \varepsilon_n + i0}, \tag{3}$$

where V is the electron-positron Coulomb interaction, the sum runs over all intermediate positron states ν, excited electron states μ, and hole states n, and $i0$ is an infinitesimal positive imaginary quantity.

It is easy to see from Eq. (3) that at low energies E the diagonal matrix element $\langle\varepsilon|\Sigma_E^{(2)}|\varepsilon\rangle$ is negative. This means that the second-order contribution to the correlation potential, Fig. 1(a), describes attraction. In fact, this diagram accounts for the main correlation effect in low-energy scattering, namely the polarization of the atom by the charged projectile. At large distances it leads to a well-known local polarization potential,

$$\Sigma_E^{(2)}(\mathbf{r},\mathbf{r}') \sim -\frac{\alpha}{2r^4}\delta(\mathbf{r} - \mathbf{r}'), \tag{4}$$

where α is the static dipole polarizability of the atom in the HF approximation,

$$\alpha = \frac{2}{3}\sum_{\mu,n} \frac{|\langle\mu|\mathbf{r}|n\rangle|^2}{\varepsilon_\mu - \varepsilon_n}. \tag{5}$$

Besides the second-order diagram, Fig. 1 shows the main third-order contributions. A complete list of third-order diagrams includes mirror images of the diagrams (f) and (g). There are also a few more diagrams similar to diagram (h), where the positron line is connected to the atomic excitation
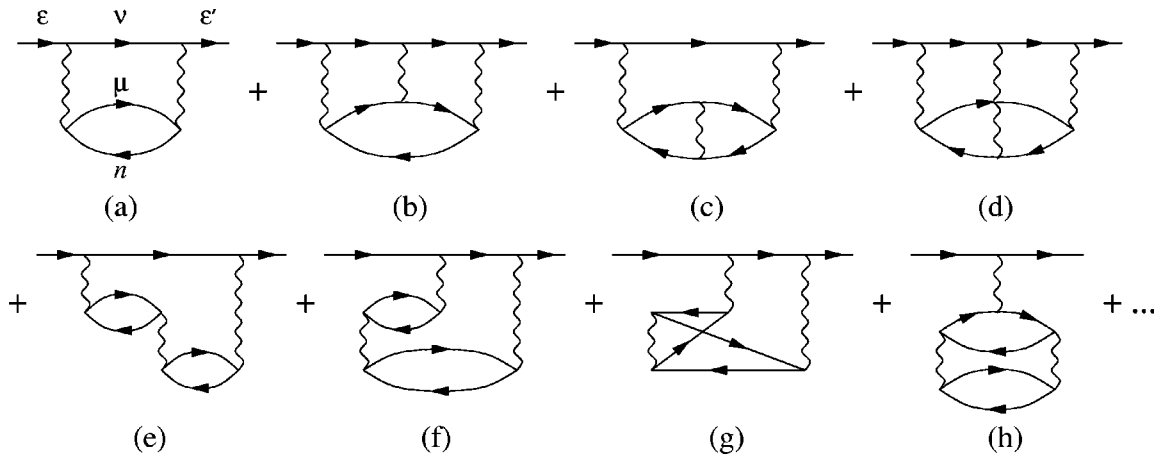
FIG. 1. Diagrammatic expansion of the positron-atom correlation potential Σ. Shown are the second-order and main third-order contributions. The top line in all the diagrams corresponds to the positron. Other lines with the arrows to the right describe *excited* electron states, while those with the arrows to the left correspond to holes, i.e., the electron states *occupied* in the atomic ground state. Wavy lines are the electron-positron or electron-electron Coulomb interactions.

part by a single line. They represent correlation corrections to the HF electron charge density of the ground-state atom. Such corrections are much smaller than other correlations effects [34], and can be neglected. The total number of the third-order diagrams in the positron-atom problem is considerably smaller than that in the electron case (see, e.g., Ref. [34]), where one needs to allow for the exchange between the incident and core electrons.

Comparing diagrams (c), (e), (f) and (g) with (a) in Fig. 1, we see that they represent corrections to the leading polarization diagram $\Sigma^{(2)}$, due to electron correlations within the atom. Interaction between electron-hole pairs can in principle be included in all orders, which would correspond to the random-phase approximation (RPA) treatment of atomic polarization [46]. On the other hand, if the two hole orbitals in diagrams (c) and (e) are identical, these diagrams together with similar higher-order terms, are easily incorporated within the second-order diagram by calculating the excited electron states μ in the field of the atom with a hole in this orbital [25]. These approximations, and even the "bare" second-order approximation (with exchange diagrams added in both cases), give good results in electron-atom scattering and negative ion problems [26,27,29–32].

However, for the positron-atom problem the approximation based on diagrams (a) and corrections of types (c), (e), (f), and (g), proved to be deficient [2–4]. In addition one must include the diagram Fig. 1(b) and higher-order diagrams in which the positron interacts with the excited electron in the intermediate state, Fig. 2. This sequence of diagrams accounts for virtual Ps formation. It is important that it

is summed to all orders, since in quantum mechanics a bound state (here, Ps) which is absent in the zeroth approximation cannot be described by a finite number of perturbation theory terms.

Summation of the diagrammatic sequence shown in Fig. 2 is done by calculating the electron-positron *vertex function* Γ, defined here as the sum of the electron-positron ladder diagrams, Fig. 3, and denoted in the diagram by the shaded block.

Comparing the left- and right-hand sides of the diagrammatic equation in Fig. 3, we see that the vertex function satisfies the following linear equation:

$$\langle \nu_2 \mu_2 | \Gamma_E | \mu_1 \nu_1 \rangle = \langle \nu_2 \mu_2 | V | \mu_1 \nu_1 \rangle$$
$$+ \sum_{\nu, \mu} \frac{\langle \nu_2 \mu_2 | V | \mu \nu \rangle \langle \nu \mu | \Gamma_E | \mu_1 \nu_1 \rangle}{E - \varepsilon_\nu - \varepsilon_\mu + i0}. \quad (6)$$

The vertex function depends on the energy E. It has the meaning of the electron-positron scattering amplitude in the field of the atom. In the lowest-order approximation $\Gamma_E = V$.

Once the vertex function is found, the contribution of virtual Ps to the correlation potential, Fig. 2, is obtained as

$$\langle \varepsilon' | \Sigma_E^{(\Gamma)} | \varepsilon \rangle$$
$$= \sum_{\nu_i, \mu_i, n} \frac{\langle \varepsilon' n | V | \mu_2 \nu_2 \rangle \langle \nu_2 \mu_2 | \Gamma_{E+\varepsilon_n} | \mu_1 \nu_1 \rangle \langle \nu_1 \mu_1 | V | n \varepsilon \rangle}{(E - \varepsilon_{\nu_2} - \varepsilon_{\mu_2} + \varepsilon_n + i0)(E - \varepsilon_{\nu_1} - \varepsilon_{\mu_1} + \varepsilon_n + i0)}. \quad (7)$$

Since the electron-positron Coulomb interaction is attractive,
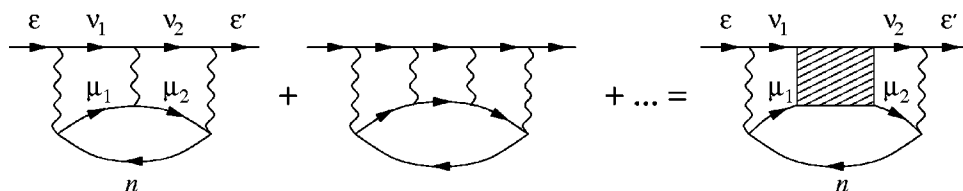

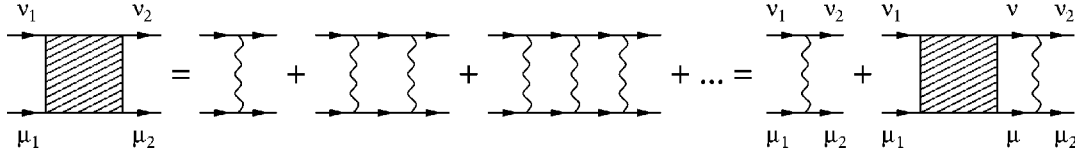FIG. 2. Virtual Ps contribution to the positron-atom correlation potential Σ.

FIG. 3. Electron-positron ladder diagram sequence and its sum, the vertex function Γ.

$V < 0$, the terms of the perturbation series in Fig. 3 have the same sign. This explains why their sum, and hence the contribution of virtual Ps formation to the positron-atom attraction, are large. Note that for electron scattering ($V > 0$) this series is alternating. As a result the net contribution of the diagrammatic series on the left-hand side in Fig. 2 is small, and its omission in the electron-atom correlation potential does not give rise to large errors.

The Ps-formation contribution to the correlation potential was previously approximated by using the free $1s$-state Ps propagator orthogonalized to the ground-state electron wave functions [4,36],

$$\langle \varepsilon' | \Sigma_E^{(\Gamma)} | \varepsilon \rangle \approx \sum_n \int \frac{\langle \varepsilon' n | V | \tilde{\Psi}_{1s,\mathbf{K}} \rangle \langle \tilde{\Psi}_{1s,\mathbf{K}} | V | n \varepsilon \rangle}{E + \varepsilon_n - E_{1s} - K^2/4 + i0} \frac{d\mathbf{K}}{(2\pi)^3},$$

(8)

where $\Psi_{1s,\mathbf{K}} = (8\pi)^{-1/2} \exp(-|\mathbf{r} - \mathbf{r}'|/2) \exp[i\mathbf{K} \cdot (\mathbf{r} + \mathbf{r}')/2]$ is the wave function of Ps($1s$) with momentum $\mathbf{K}$, $E_{1s} + K^2/4$ is the energy of this state, and the tilde above $\Psi_{1s,\mathbf{K}}$ in Eq. (8) indicates orthogonalization. This approximation is suitable for positron scattering from the targets where ground-state Ps formation dominates, e.g., hydrogen or noble gas atoms. It also allows one to consider positron scattering above the Ps-formation threshold, where the correlation potential acquires an imaginary part due to the pole in the integral in Eq. (8) [37,47]. At the same time, the ground-state Ps propagator fails to describe the short-range electron-positron correlations crucial for the calculation of the annihilation rates [36]. By the uncertainty principle, small separations invoke contributions of highly excited states of the Ps internal motion, not included in the Ps($1s$) propagator. In contrast, our present method based on the summation of the ladder diagram series, Eqs. (6) and (7), is consistent and complete. It accounts for all (virtual) intermediate states of the electron-positron pair.

For positron scattering on hydrogen, only a few types of diagrams contribute to Σ_E, since only one hole can be created. Moreover, the interaction of the intermediate-state electron and positron with the hole [diagrams (c) and (d) in Fig. 1] can be taken into account by calculating the intermediate electron and positron wave functions in the Coulomb field of the nucleus. In this case, the correlation potential is given by the sum of the second-order diagram and the virtual Ps contribution, Figs. 1(a) and 2, and

$$\Sigma_E = \Sigma_E^{(2)} + \Sigma_E^{(\Gamma)}$$

(9)

is the *exact* correlation potential. In particular, the long-range asymptotic behavior of $\Sigma_E^{(2)}$ at low energies, Eq. (4), contains the exact polarizability of hydrogen, $\alpha = \frac{9}{2}$.

C. Scattering

Rather than solving the Dyson equation for the quasiparticle wave function in the coordinate representation, it is easier to work with the self-energy matrix,

$$\langle \varepsilon' | \Sigma_E | \varepsilon \rangle = \int \varphi_{\varepsilon'}^*(\mathbf{r}) \Sigma_E(\mathbf{r}, \mathbf{r}') \varphi_\varepsilon(\mathbf{r}') d\mathbf{r} d\mathbf{r}',$$

(10)

where φ_ε are the positron eigenfunctions of the HF (or ground-state hydrogen) Hamiltonian H_0,

$$H_0 \varphi_\varepsilon = \varepsilon \varphi_\varepsilon,$$

(11)

with a given angular momentum l, $\varphi_\varepsilon(\mathbf{r}) = r^{-1} P_{\varepsilon l}(r) Y_{lm}(\Omega)$. Since the static potential of the atom is repulsive, all positron states φ_ε lie in the continuum ($\varepsilon > 0$). The radial wave functions are normalized to a δ function of energy in Rydberg, $\delta(k^2 - k'^2)$, where k is the positron momentum. This corresponds to the asymptotic behavior

$$P_{\varepsilon l}(r) \sim (\pi k)^{-1/2} \sin(kr - l\pi/2 + \delta_l^{(0)}),$$

(12)

where $\delta_l^{(0)}$ is the scattering phase shift in the static potential.

The matrix (10) can be used to obtain the phase shifts directly [26]. First, a "reducible" self-energy matrix $\langle \varepsilon' | \tilde{\Sigma}_E | \varepsilon \rangle$ is found via the integral equation,

$$\langle \varepsilon' | \tilde{\Sigma}_E | \varepsilon \rangle = \langle \varepsilon' | \Sigma_E | \varepsilon \rangle + P \int \frac{\langle \varepsilon' | \tilde{\Sigma}_E | \varepsilon'' \rangle \langle \varepsilon'' | \Sigma_E | \varepsilon \rangle}{E - \varepsilon''} d\varepsilon'',$$

(13)

where P means the principal value of the integral. The phase shift is then given by

$$\delta_l = \delta_l^{(0)} + \Delta \delta_l,$$

(14)

where

$$\tan \Delta \delta_l = -2\pi \langle \varepsilon | \tilde{\Sigma}_\varepsilon | \varepsilon \rangle,$$

(15)

determines the additional phase shift $\Delta \delta_l(k)$ due to correlations, at the positron energy ε.

Once the reducible self-energy matrix has been found, the quasiparticle wave function (also known as the *Dyson orbital*) can be found via

$$\psi_\varepsilon(\mathbf{r}) = \varphi_\varepsilon(\mathbf{r}) + P \int \varphi_{\varepsilon'}(\mathbf{r}) \frac{\langle \varepsilon' | \tilde{\Sigma}_\varepsilon | \varepsilon \rangle}{\varepsilon - \varepsilon'} d\varepsilon'.$$

(16)

In order to normalize the quasiparticle radial wave function at large distances to
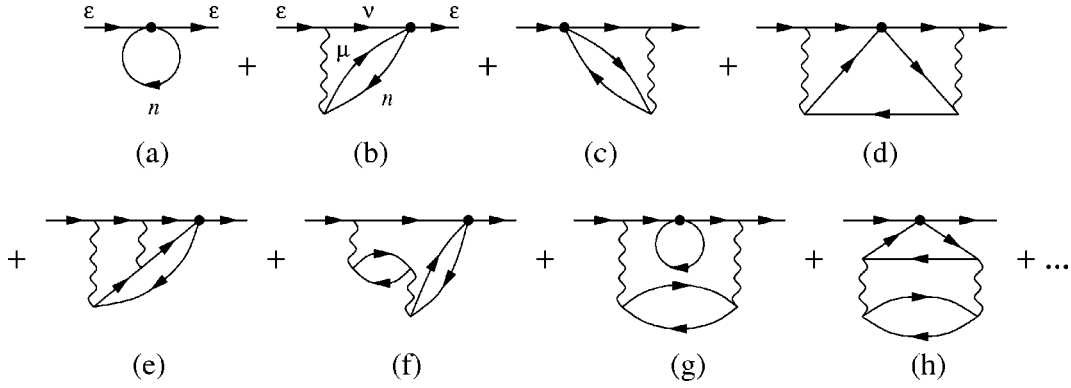
FIG. 4. Diagrammatic expansion of Z_{eff}. Apart from the zeroth and first-order diagrams (a), (b), and (c), the main types of second-order diagrams are shown. The external lines of these diagrams (ε) represent the wave function of the incident positron. The solid circle corresponds to the electron-positron δ-function annihilation vertex.

$$\tilde{P}_{\varepsilon l}(r) \sim (\pi k)^{-1/2} \sin(kr - l\pi/2 + \delta_l^{(0)} + \Delta\delta_l), \quad (17)$$

the function obtained from the right-hand side of Eq. (16) must be multiplied by the factor

$$\cos\Delta\delta_l = [1 + (2\pi\langle\varepsilon|\tilde{\Sigma}_\varepsilon|\varepsilon\rangle)^2]^{-1/2}. \quad (18)$$

D. Positron annihilation

The annihilation rate λ of a positron in a gas of number density n is usually expressed in terms of the effective number of electrons Z_{eff}, which contribute to annihilation on an atom or molecule [48,49],

$$\lambda = \pi r_0^2 cnZ_{eff}, \quad (19)$$

where r_0 is the classical electron radius and c is the speed of light. Equation (19) defines Z_{eff} as the ratio of the positron two-photon annihilation cross section of the atom to the spin-averaged two-photon annihilation cross section of a free electron in the Born approximation [50]. Annihilation takes place at very small electron-positron separations, $\hbar/(mc)$ $\sim 10^{-2}$ a.u. Hence for nonrelativistic positrons it is determined by the electron density at the positron, and Z_{eff} can be calculated as [48],

$$Z_{eff} = \sum_{i=1}^{N} \int |\Psi(\mathbf{r}_1, \mathbf{r}_2, \ldots, \mathbf{r}_N, \mathbf{r})|^2 \delta(\mathbf{r}_i - \mathbf{r}) d\mathbf{r}_1 \cdots d\mathbf{r}_N d\mathbf{r}, \quad (20)$$

where $\Psi(\mathbf{r}_1, \mathbf{r}_2, \ldots, \mathbf{r}_N, \mathbf{r})$ is the full $(N+1)$-particle wave function of the N electron coordinates $\mathbf{r}_i$ and positron coordinate $\mathbf{r}$. The wave function is normalized to a positron plane wave at large positron-atom separations,

$$\Psi(\mathbf{r}_1, \mathbf{r}_2, \ldots, \mathbf{r}_N, \mathbf{r}) \simeq \Phi_0(\mathbf{r}_1, \mathbf{r}_2, \ldots, \mathbf{r}_N)e^{i\mathbf{k}\cdot\mathbf{r}}, \quad (21)$$

where $\Phi_0(\mathbf{r}_1, \mathbf{r}_2, \ldots, \mathbf{r}_N)$ is the atomic ground-state wave function, and $\mathbf{k}$ is the incident positron momentum.

Although Z_{eff} is basically a cross section, Eq. (20) has the form of a transition amplitude. This enables one to apply the

apparatus of many-body theory to this quantity directly [3,36]. In this "transition amplitude" the initial and final states are identical, and the electron-positron two-body operator, $\Sigma_i\delta(\mathbf{r}_i - \mathbf{r})$, plays the role of a perturbation. The positron energy in the initial and final states is the same, $\varepsilon = k^2/2$, and (owing to the spherical symmetry of the target) the perturbation conserves the positron angular momentum l. Therefore the contribution of each positron partial wave to Z_{eff} can be determined separately. The corresponding many-body diagrammatic expansion is presented in Fig. 4.

The analytical expression for the zeroth-order diagram, Fig. 4(a), is

$$Z_{eff}^{(0)} = \sum_n \int \psi_\varepsilon^*(\mathbf{r})\varphi_n^*(\mathbf{r}_1)\delta(\mathbf{r} - \mathbf{r}_1)\varphi_n(\mathbf{r}_1)\psi_\varepsilon(\mathbf{r})d\mathbf{r}d\mathbf{r}_1$$

$$= \sum_n \int |\varphi_n(\mathbf{r})|^2|\psi_\varepsilon(\mathbf{r})|^2 d\mathbf{r}, \quad (22)$$

where ψ_ε is the positron wave function, φ_n is the wave function of the hole, and the sum over n runs over all holes, i.e., orbitals occupied in the target ground state. This contribution is simply an overlap of the electron and positron densities, $\Sigma_n|\varphi_n(\mathbf{r})|^2$ and $|\psi_\varepsilon(\mathbf{r})|^2$, respectively.

The two first-order "corrections," Figs. 4(b) and 4(c), are identical, and their contribution is

$$Z_{eff}^{(1)} = 2\sum_{\nu,\mu,n} \frac{\langle\varepsilon n|\delta|\mu\nu\rangle\langle\nu\mu|V|n\varepsilon\rangle}{\varepsilon - \varepsilon_\nu - \varepsilon_\mu + \varepsilon_n}, \quad (23)$$

cf. Eq. (3) for the second-order contribution to the correlation potential. In the calculations of annihilation we assume that the positron energy is below all other inelastic thresholds, hence we have dropped $i0$ in the energy denominator. Physically, the first-order diagram describes positron annihilation with an electron "pulled out" from the atom by the positron's Coulomb field. Calculations in Refs. [3,36] showed that for noble-gas atoms the size of the first-order corrections is approximately equal to the zeroth-order contribution. This means that higher-order terms must also be taken into account.
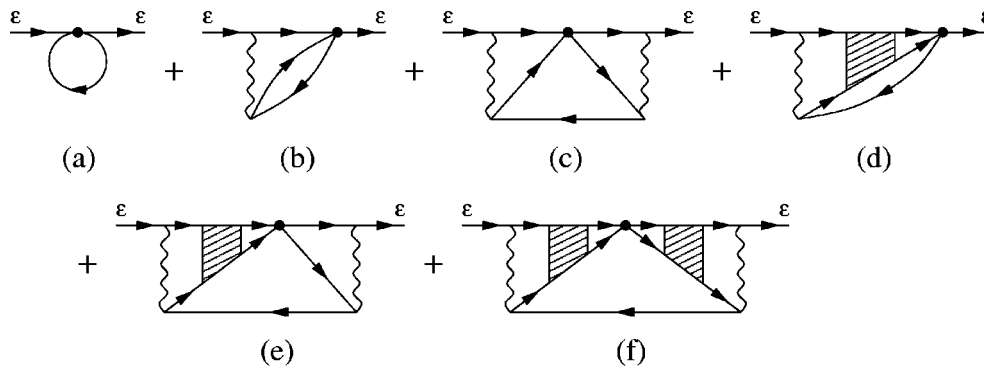
FIG. 5. Main contributions to the positron-atom annihilation parameter Z_{eff}. To account for the mirror images of the diagrams (b), (d), and (e), their contributions are multiplied by 2.

Diagrams (d)–(h) in Fig. 4 illustrate the main types of second-order corrections to the *annihilation vertex*. It is also important to consider corrections to the incident positron wave functions denoted by ε. However, these corrections are included in all orders in the positron quasiparticle wave function, obtained from the Dyson equation (1), or via Eq. (16). Hence their contribution to Z_{eff} is accounted for by using the positron Dyson orbitals ψ_ε in the calculation of the annihilation diagrams.

The presence of the δ-function operator in the annihilation diagrams enhances the importance of small electron-positron separations. For this reason, the most important diagrams in Z_{eff} are those with the Coulomb interactions between the annihilating pair, e.g., the second-order diagrams (d) and (e) in Fig. 4 (the latter together with its mirror image), and similar higher-order terms. A complete all-order calculation of their contribution is achieved by using the vertex function, as shown in Fig. 5. Note that for hydrogen this set of diagrams is exhaustive, provided the intermediate electron and positron states are calculated in the field of the bare nucleus. Previously diagrams (c)–(f) in Fig. 5 have only been estimated [36]. We will see that the ability to calculate these diagrams accurately is crucial for obtaining correct values of Z_{eff}. We will also see in Sec. IV that the role of the vertex function (representing virtual Ps) in annihilation is much greater than in scattering.

Of course, for many-electron targets one can also consider other diagrams, e.g., (f)–(h) in Fig. 4. In particular, diagram (f) describes screening of the electron-positron Coulomb interaction by other electrons [cf. Fig. 1(e)]. Diagram (g) can be viewed as the lowest-order "pick-off" annihilation contribution. Here the positron excites an electron-hole pair (a precursor of virtual Ps formation) and annihilates with an electron from one of the ground-state orbitals. Diagram (h) is independent of the positron energy. It represents one of the corrections to the HF ground-state electron density, cf. Fig. 1(h). Unlike the diagrams in Fig. 5, these contributions are not systematically enhanced by the electron-positron Coulomb interaction at small distances.

It is clear from Fig. 4 that most correlation corrections to the annihilation vertex, including the dominant sequence of

diagrams in Fig. 5, are *nonlocal*. As a result, the total Z_{eff} can be written as

$$Z_{eff} = \int \sum_n |\varphi_n(\mathbf{r})|^2 |\psi_\varepsilon(\mathbf{r})|^2 d\mathbf{r} + \int \psi_\varepsilon^*(\mathbf{r})\Delta_\varepsilon(\mathbf{r},\mathbf{r}')\psi_\varepsilon(\mathbf{r}')d\mathbf{r}d\mathbf{r}',$$

(24)

where $\Delta_\varepsilon(\mathbf{r},\mathbf{r}')$ represents the nonlocal correlation correction to the annihilation vertex. In the approximation of Fig. 5, it is equal to the sum of all diagrams (b)–(f) with the external positron lines ε detached. Diagram (h) in Fig. 4 and similar diagrams which represent corrections to the HF electron density could be included by replacing of the HF electron density $\sum_n |\varphi_n(\mathbf{r})|^2$ in Eq. (24) with the exact target electron density $\rho_e(\mathbf{r})$. Given the high accuracy of the HF density, this would make only a small change in Z_{eff}. The structure of Eq. (24) shows that even when one uses the best single-particle positron wave function, the annihilation rate is not reduced to a simple (local) overlap of the electron and positron densities.

There is an important physical difference between the correlation effects in positron scattering and annihilation. The key role played by the long-range polarization potential for low-energy positrons means that large distances are important. Polarization also emphasizes the role played by the dipole part of the positron-target Coulomb interaction and dipole target excitations. The contribution of virtual Ps formation to Σ_E is a short-range effect. The typical distances here are comparable to the radius of the atom, or the radius of ground-state Ps. The net effect of the strong positron-atom attraction brings about low-lying virtual s states (see, e.g., Ref. [44]) for Ar, Kr, and Xe [36], or positron-atom weakly bound states, e.g., in Mg [35,37]. In both cases, the positron scattering phase shifts and the positron quasiparticle wave function in the vicinity of the atom vary rapidly as functions of the positron energy.

On the contrary, in the annihilation diagrams the δ-function vertex emphasises small electron-positron separations. By the uncertainty principle, such small separations correspond to high-energy excitations in the intermediate states in the diagrams (b)–(f), Fig. 5. As a result, the nonlocal correction to the annihilation vertex, Δ_ε, has a weak energy

dependence, and the energy dependence of the second term in Eq. (24) is almost entirely due to that of the positron wave functions. The only exception is when the positron energy approaches the Ps-formation threshold from below. Here the virtual-Ps contribution, Fig. 5(f), rises sharply. Details of the threshold behavior of Z_{eff} are discussed in Ref. [51].

The large difference in the energy scales characteristic of positron scattering and annihilation has another physically important consequence. It turns out that the *relative* size of the annihilation vertex corrections in Z_{eff}, i.e., the ratio of the second term in Eq. (24) to $Z_{\text{eff}}^{(0)}$, is about the same, whether ψ_ε are the positron wave functions in the repulsive static potential, $\psi_\varepsilon = \varphi_\varepsilon$, or the Dyson orbitals which fully account for the positron-atom correlation potential. Numerical illustrations of this effect will be provided in Sec. IV.

Finally, we should mention that the correct normalization of Z_{eff} for positrons with angular momentum l is obtained by multiplying the diagrams in Figs. 4 and 5 by the extra numerical factor,

$$\frac{4\pi^2}{k}(2l+1).\tag{25}$$

This follows from the structure of the positron wave function $\psi_{\mathbf{k}}$, which has the asymptotic behavior of a plane wave $e^{i\mathbf{k}\cdot\mathbf{r}}$ at large distances [cf. Eq. (21)],

$$\psi_{\mathbf{k}} = \frac{4\pi}{r}\sqrt{\frac{\pi}{k}}\sum_{l=0}^{\infty}\sum_{m=-l}^{m=l} i^l e^{i\delta_l}\widetilde{P}_{\varepsilon l}(r)Y_{lm}^*(\Omega_{\mathbf{k}})Y_{lm}(\Omega_{\mathbf{r}}).\tag{26}$$

To derive Eq. (25), one can use $\psi_{\mathbf{k}}$ as the external positron lines in an annihilation diagram, and perform averaging over the directions of $\mathbf{k}$.

III. NUMERICAL IMPLEMENTATION

A. Use of *B* splines and convergence

To evaluate the diagrams of the correlation potential Σ and annihilation parameter Z_{eff}, one first needs to generate sets of electron and positron HF basis states. These are then used to calculate matrix elements of the Coulomb and δ-function operators, the main building blocks of the diagrams. Evaluation of the diagrams requires summation over complete sets of electron and positron intermediate states, including integration over the electron and positron continua.

To perform a numerical calculation, the continuous spectrum can be discretized. The simplest way of doing this is by placing the system in a spherical cavity of radius R. Setting the wave functions to zero at the boundary will result in a discrete spectrum of eigenstates with an approximately constant step size in momentum space,

$$\Delta k \approx \pi/R.\tag{27}$$

If the value of R is sufficiently large ($R \gg R_{\text{at}}$, where $R_{\text{at}} \sim 1$ a.u. is the size of the atom), the presence of the boundary will not affect the quantities calculated. Indeed, for the positron energy below all inelastic thresholds (except, of course, annihilation), the intermediate states in the diagrams are *virtual*, and no particle in an intermediate state can escape to infinity.

The drawback of this procedure is that for a suitably large R, the step size in momentum is small, e.g., for $R=30$ a.u., $\Delta k \approx 0.1$ a.u. Hence one would need large numbers of intermediate states to achieve convergence. Note that the actual upper energy limit depends on the quantity in question. Thus diagrams in Z_{eff} converge more slowly than those of the correlation potential Σ, because of the greater role of small electron-positron separations and high orbital angular momenta in the former. However, as a rough guide, summing up to the energy of 10^2 a.u. should be sufficient for both. The question of the number of intermediate states is especially important for the calculation of the vertex function Γ, which is a $N_\Gamma \times N_\Gamma$ matrix [see Eq. (6)], where $N_\Gamma \sim N^2(l_{\max}+1)$, N being the number of electron or positron states in each partial wave and $l_{\max}$ being the largest orbital angular momentum included. It is clear that here the simple cavity quantization cannot work.

Instead, to achieve an accurate and economical span of the continuum we use B splines [52]. B splines of order k are n piecewise polynomials of degree $k-1$ defined by a knot sequence r_j which divides the interval $[0,R]$ into $n-k+1$ segments [53]. The basis states are obtained by expanding the radial wave functions $P_l(r)$ in terms of B splines $B_i(r)$,

$$P_l(r) = \sum C_i^{(l)}B_i(r),\tag{28}$$

and finding the eigenvectors and eigenvalues of the radial part of the HF (or hydrogen atom) Hamiltonian for each orbital angular momentum l by solving the generalized eigenvalue problem,

$$\sum H_{ij}C_j^{(l)} = \varepsilon \sum Q_{ij}C_j^{(l)},\tag{29}$$

where $H_{ij} = \langle B_i|H_0^{(l)}|B_j\rangle$, and $Q_{ij} = \langle B_i|B_j\rangle$. Prior to solving Eq. (29), the ground-state atom HF Hamiltonian is generated by a conventional HF routine [54]. Note that in the sums over i and j in Eqs. (28) and (29) the first and last splines are discarded to implement the boundary condition $P_l(0) = P_l(R) = 0$, leaving one with a set of $n-2$ eigenstates for each electron and positron orbital angular momentum. When Eq. (29) is solved for the electron, it yields the wave functions of the orbitals occupied in the atomic ground state (holes), as well as those of the excited states (particles). The exact energies of the excited electron and positron states are determined by the B-spline radial knot sequence.

It is instructive to try to design an ideal distribution of energies of a discrete set spanning the continuum. Qualitatively, at low energies ($\varepsilon \ll 1$ a.u.) the continuous spectrum states oscillate slowly, and the contribution of large distances in the matrix elements is important (hence the need for a large R). As the energy of the states increases, the range of important distances becomes smaller and smaller. Indeed, the matrix elements then contain rapidly oscillating factors of e^{ikr} type, which means that the dominant contribution comes from $r \lesssim k^{-1}$. Therefore one does not need a large value of the cavity radius R for the higher-energy states. More specifically, one can estimate the necessary radius as $R \sim a/k$, where a is a number greater than unity. Combining this with the cavity quantisation condition (27), one obtains $\Delta k/k \sim \pi/a$, which yields the following grid in momentum space:
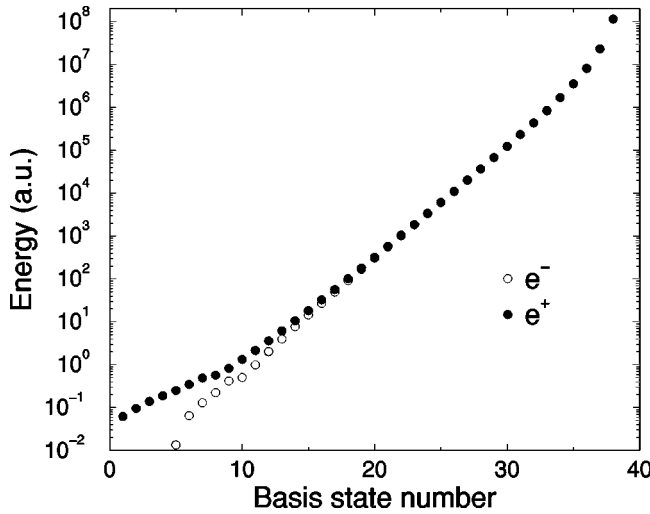
FIG. 6. Energies of the electron (open circles) and positron (solid circle) s-wave B-spline basis states in the field of the hydrogen nucleus, obtained using $R=30$, $k=6$, and $n=40$. The first four electron states with negative energies ($-0.500\,00$, $-0.125\,00$, $-0.055\,42$, and $-0.002\,46$ a.u.) are not shown.

$$k_j = k_0 e^{\beta j}, \tag{30}$$

where k_0 is the lowest momentum, $\beta = \pi/a$, and $j = 0, 1, 2, \dots$. Thus it appears that the optimal momentum and energy grids are exponential. By choosing a small initial momentum $k_0 \ll 1$ a.u. and $\beta < 1$ one ensures that the stepsize in momentum, $\Delta k \approx \beta k$, is sufficiently small, to describe accurately the energy variation of the quantities summed.

It turns out that basis sets generated by Eqs. (28) and (29) using an exponential radial knot sequence [52] are a very close realization of the exponential energy grid, and are *effectively complete*. In the present work we use $n=40$ B splines of order $k=6$ with a knot sequence

$$r_j = \rho(e^{\sigma j} - 1), \tag{31}$$

where $\rho = 10^{-3}$ a.u., and σ is determined by the condition $r_{n-k+1} = R$. Figure 6 shows the positive eigenenergies of the electron and positron basis states with $l=0$ for the hydrogen atom. Their distribution does indeed correspond to the exponential ansatz, Eq. (30), with $\beta \approx \sigma$. The highest energies in the sets are about 10^8 a.u. This value is close to the magnitude of $(\rho\sigma)^{-2}$, since the knot point closest to the origin determines the most rapidly varying eigenstate (by the uncertainty principle). In fact, it may not be necessary to include all 38 basis states in each partial wave in the many-body theory sums. In the calculations reported in this paper we use only about 15 lowest states, which span the energy range from threshold to $\sim 10^2$ a.u.

Note that B-spline basis sets are used widely in atomic physics [52], and that there are other basis sets which show a near-exponential spanning of the continuum. In particular, Laguerre basis states provide rapid convergence in close-coupling electron-atom scattering calculations [55].

B. Calculation of the self-energy and annihilation diagrams

The self-energy and annihilation diagrams are calculated by summation over the B-spline basis states, and the vertex function is found by matrix inversion from Eq. (6). The angular parts of the states are separated in the matrix elements and the angular variables are integrated over analytically. The actual expressions for the diagrams are given in the Appendix. The self-energy matrix and the vertex function are energy dependent. In practice, the self-energy matrix has been calculated at eight energies spaced evenly from zero to the Ps formation threshold. Interpolation onto any required energy E is then used.

Apart from the B-spline basis states, we also consider true positron continuum HF states (12). They are needed to evaluate the matrix elements $\langle\varepsilon|\Sigma_E|\varepsilon'\rangle$ and obtain the phase shifts via Eqs. (13)–(15). Here we use 201 states that form an equidistant mesh in positron momenta of size $\Delta k = 0.02$. A transformation of the B-spline basis matrix elements $\langle i|\Sigma_E|j\rangle$ into $\langle\varepsilon|\Sigma_E|\varepsilon'\rangle$ could be done using the effective completeness of the B-spline states on the interval $[0,R]$,

$$\langle\varepsilon|\Sigma_E|\varepsilon'\rangle = \sum_{i,j} \langle\varepsilon|i\rangle\langle i|\Sigma_E|j\rangle\langle j|\varepsilon'\rangle, \tag{32}$$

where $\langle\varepsilon|i\rangle$ is the overlap of the HF state with the B-spline basis state. However, unlike the B-spline states which satisfy the zero boundary condition at $r=R$, the continuous spectrum state $P_{\varepsilon l}$ is finite at the boundary. To fix this problem we insert a radial weighting function $f(r) = R - r$ into Eq. (32), which now reads

$$\langle\varepsilon|\Sigma_E|\varepsilon'\rangle = \sum_{i,j} \langle\varepsilon|f|i\rangle\langle i|f^{-1}\Sigma_E f^{-1}|j\rangle\langle j|f|\varepsilon'\rangle, \tag{33}$$

and calculate the "weighted" self-energy matrix $\langle i|f^{-1}\Sigma_E f^{-1}|j\rangle$, rather than $\langle i|\Sigma_E|j\rangle$. The singularity of f^{-1} at $r=R$ does not cause a problem, since the B-spline basis states in the Coulomb matrix elements involved, vanish at $r=R$. The same trick is applied in the calculation of the annihilation diagrams.

To calculate $\langle\varepsilon|\Sigma_E|\varepsilon'\rangle$ more accurately at low positron energies, where distances beyond $r=R$ can be important, we make use of the long-range asymptotic form of the correlation potential (4). The contribution of $r>R$ can be evaluated as

$$\int_R^\infty P_{\varepsilon l}(r)\left(-\frac{\alpha}{2r^4}\right)P_{\varepsilon' l}(r)dr, \tag{34}$$

with the correct value of the dipole polarizability α, and added to $\langle\varepsilon|\Sigma_E|\varepsilon'\rangle$.

C. Convergence with respect to the orbital angular momenta

The use of a B-spline basis means that fast convergence is achieved with respect to the number of states with a particular orbital angular momentum. However, this leaves open the question of convergence with respect to the maximal orbital angular momentum of the electron and positron intermediate

states included in the calculation. It has been known for a while that calculations of positron-atom scattering converge slowly with respect to the number of target angular momenta included in the expansion of the total wave function, notably slower than in the electron-atom case [56]. This is also true for the configuration-interaction-type calculations of positron-atom bound states [17,19,57] and scattering [20]. Calculations of annihilation rates converge even more slowly [19,20,57]. Physically, the slow convergence rate arises from the need to describe virtual Ps localized outside the atom by an expansion in terms of single-particle orbitals centered on the nucleus.

The problem of the convergence rate with respect to the maximal orbital angular momentum has been investigated by the authors in Ref. [58]. Using a perturbation-theory approach and the original ideas of Schwartz [59], we derived asymptotic formulas that describe the convergence of the scattering amplitudes, or the phase shifts, and annihilation rates, or Z_{eff}. The contribution of high orbital angular momenta probes small particle separations in the system. The difference between the convergence rates of the scattering and annihilation parameters is due to the presence of either the Coulomb interaction or the δ-function annihilation operator in the relevant amplitudes.

The increments to the phase shifts and Z_{eff} upon increasing the maximum orbital angular momentum from $\lambda - 1$ to λ, were found to behave as $(\lambda + 1/2)^{-4}$ and $(\lambda + 1/2)^{-2}$, respectively. This means that if a series of calculations is stopped at some maximal angular momentum $\lambda = l_{max}$, the values obtained approach the ultimate ($l_{max} \to \infty$) values as follows:

$$\delta_l^{[l_{max}]} \simeq \delta_l - \frac{A}{(l_{max} + 1/2)^3}, \qquad (35)$$

$$Z_{eff}^{[l_{max}]} \simeq Z_{eff} - \frac{B}{(l_{max} + 1/2)}, \qquad (36)$$

where A and B are some constants. They are determined together with δ_l and Z_{eff} by fitting Eqs. (35) and (36) to the numerical data obtained for a range of l_{max}. This extrapolation to $l_{max} \to \infty$ is performed at each positron momentum value considered, and is especially important for obtaining correct values of Z_{eff}.

IV. RESULTS: SCATTERING AND ANNIHILATION ON HYDROGEN

The theory outlined above can be readily applied to any closed-shell atom or ion. In this paper we would like to test it for the simplest possible target, the hydrogen atom. Since it contains only one electron, the correlation potential from Eq. (9) and the Z_{eff} diagrams in Fig. 5 give an exact solution of the elastic scattering and annihilation problems, provided the intermediate electron and positron states are calculated in the field of H^+. The key advance of the present many-body theory of positron-atom interactions relates to the calculation of the electron-positron vertex function Γ, Eq. (6), and its incorporation in the self-energy and annihilation diagrams. It is mainly these features of the theory that a positron-hydrogen calculation is intended to test.

In the numerical implementation we first generate the electron and positron B-spline basis sets. They are then used to evaluate the matrix elements, find the vertex function, and calculate the self-energy and annihilation diagrams (see the Appendix). Using the self-energy matrix, the phase shifts are obtained by means of Eqs. (13)–(15), and the positron Dyson orbital is calculated from Eqs. (16) and (18). In the end, the Dyson orbitals replace the positron HF states in the external lines of the annihilation diagrams, and final values of Z_{eff} are obtained. To test the stability of the results with respect to the cavity radius, the calculations were performed with $R = 15$ and 30 a.u.

To extrapolate the scattering phase shifts and Z_{eff} to $l_{max} \to \infty$, as per Eqs. (35) and (36), the diagrams are evaluated for a range of maximal orbital angular momenta, $l_{max} = 7 - 10$. This procedure is illustrated by Fig. 7 for the phase shifts and Fig. 8 for Z_{eff}, for the s-, p-, and d-wave incident positron with momenta $k = 0.2$, 0.4, and 0.6 a.u.

Figures 7 and 8 show that the calculations have converged to the regime in which the asymptotic formula (35) for δ_l and formula (36) for Z_{eff}, may be applied. The graphs also illustrate the point that the inclusion of high orbital angular momenta and extrapolation to $l_{max} \to \infty$ is much more important in the calculations of annihilation, compared with scattering. For the positron momenta and partial waves shown, between 15% and 30% of the final value of Z_{eff} is due to such extrapolation. Quantitatively, this contribution can be characterized by the ratio B/Z_{eff}; see Eq. (36), given in Table I. Its increase with the positron angular momentum may be related to the greater role of the correlation corrections to the annihilation vertex in higher positron partial partial waves (see below).

Figure 9 shows the s-, p-, and d-wave phase shifts for the total correlation potential (9). They are in very good agreement with those from an accurate variational calculation (see Ref. [13]), the discrepancy being of order 10^{-3} rad; see also Table II. The values obtained with $R = 15$ and $R = 30$ a.u. are almost indistinguishable, except at low positron momenta. Here the results for $R = 30$ are superior to those for $R = 15$. The larger cavity size allows for a better account of the long-range $-\alpha/2r^4$ tail in the polarization potential.

Examining the phase shifts allows us to compare the relative sizes of the polarization and Ps-formation contributions to the correlation potential (9). The static positron-atom potential is repulsive, resulting in negative values of the phase shifts (thin solid curves). The inclusion of Σ, i.e., correlations, makes the low-energy phase shifts positive. Dashed curves in Fig. 9 show the phase shifts obtained by including only the second-order diagram $\Sigma^{(2)}$ (polarization), while dotted-dashed curves are those obtained with $\Sigma^{(\Gamma)}$ alone (virtual Ps formation). We see that none of these results is close to the phase shift obtained with the full Σ. This means that neither contribution dominates the correlation potential, and the inclusion of both polarization and virtual Ps-formation effects is essential for solving the positron-atom problem. Of course, any calculation which produces accurate positron-hydrogen phase shifts contains these contributions implicitly. The advantage of the many-body theory approach is that one can separate them, and get a better insight into the physics of the system.
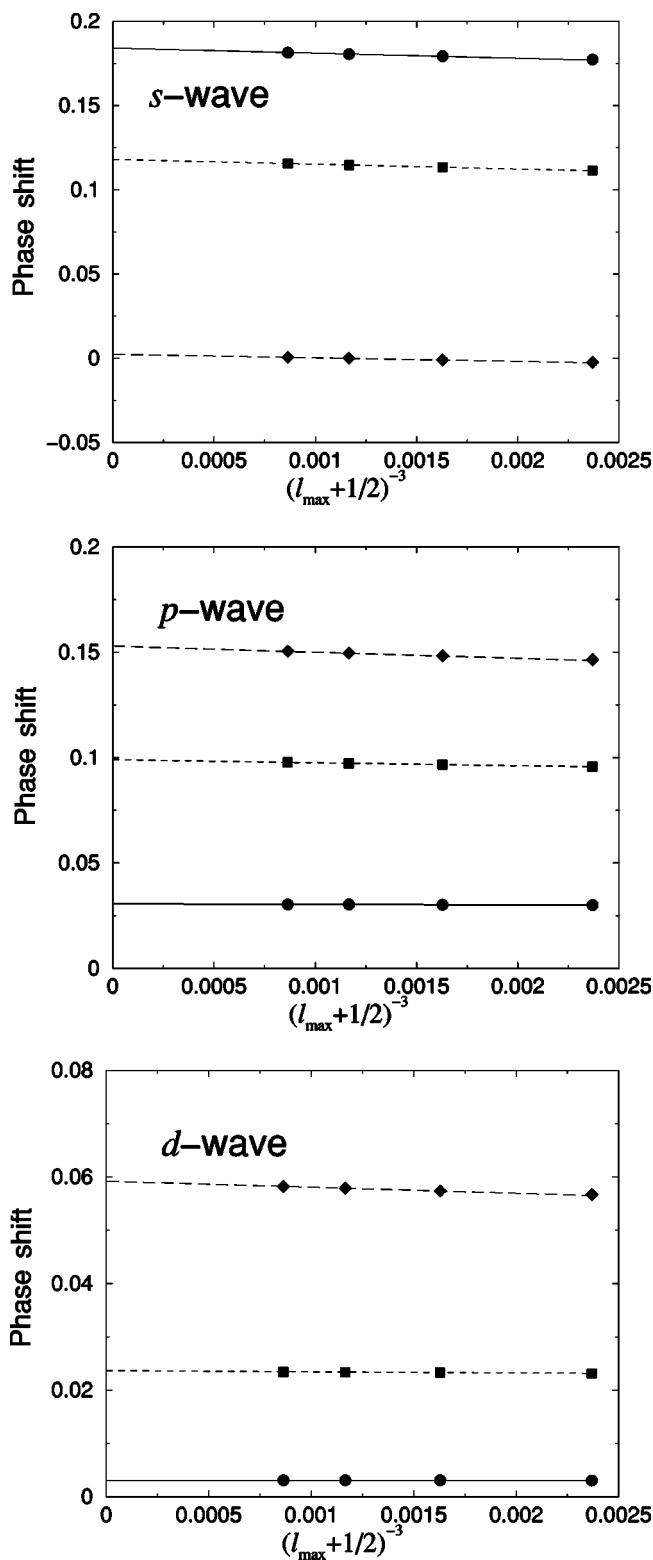
FIG. 7. Convergence of the s-, p-, and d-wave positron scattering phase shifts on hydrogen with respect to the maximal orbital angular momentum l_{max} for $R=15$ a.u. Circles, $k=0.2$ a.u.; squares, $k=0.4$ a.u.; diamonds, $k=0.6$ a.u. Lines show extrapolation.
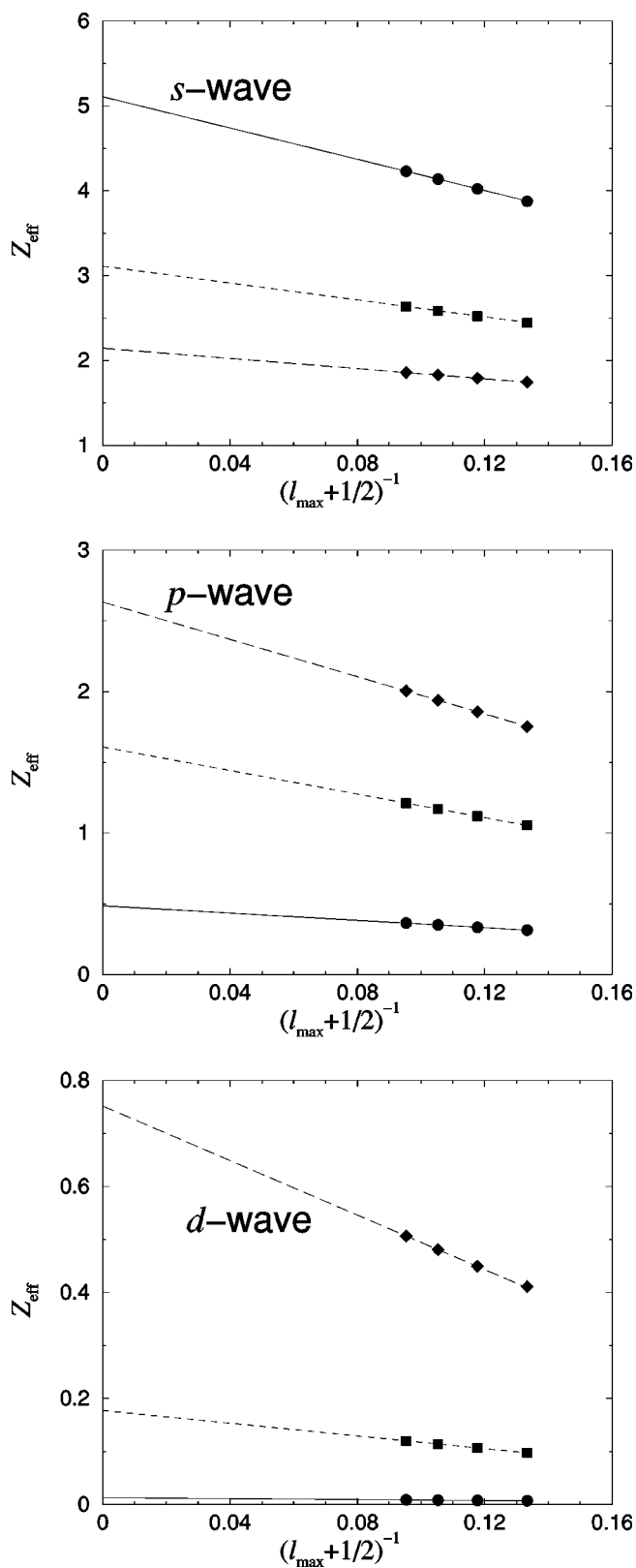
FIG. 8. Convergence of the s-, p-, and d-wave contributions to Z_{eff} for positron annihilation on hydrogen with respect to the maximal orbital angular momentum l_{max} for $R=15$ a.u. Circles, $k=0.2$ a.u.; squares, $k=0.4$ a.u.; diamonds, $k=0.6$ a.u. Lines show extrapolation.

TABLE I. Values of B/Z_{eff} which characterize the dependence of calculated Z_{eff} on l_{max}.

Momentum (a.u.)	Partial wave		
	s	p	d
0.2	1.82	2.63	3.33
0.4	1.62	2.58	3.32
0.6	1.41	2.51	3.37

To illustrate the nonperturbative nature of virtual Ps formation we have also performed calculations that include the vertex function only to first order, $\Gamma_E = V$, in $\Sigma^{(\Gamma)}$ (dotted curves in Fig. 9). This approximation accounts only for about 50% of the total vertex function contribution. Note that the higher-order terms in Γ become even more important close to the Ps formation threshold ($k \approx 0.7$) in p and d waves. This is related to the virtual Ps becoming more "real" close to the threshold.

We now turn to positron annihilation. Having solved the scattering problem accurately with the full Σ, we are now in possession of the best (quasiparticle) positron wave function, the Dyson orbital. Before using it in all annihilation diagrams, let us first look at the effect of the Dyson orbital on the zeroth-order diagram, Fig. 5(a), for the s-wave Z_{eff}. Figure 10 shows that the zeroth-order contribution, Eq. (22), evaluated with the positron wave function in the static atomic potential gives values up to 20 times smaller than the variational results of Ref. [60]. This situation is similar to that in positron annihilation on noble-gas atoms, where Eq. (22) evaluated with the static (HF) positron wave function underestimates experimental Z_{eff} by a factor of 10^1-10^3 at low positron energies [3,36]. It is natural that the use of the Dyson orbital, which is "aware" of the positron-atom attraction, in Eq. (22), leads to increased Z_{eff}, and introduces a correct momentum dependence (dashed curve in Fig. 10). This latter fact is in agreement with the general understanding of the origins of the energy dependence and enhancement of Z_{eff} at low energies, and their relation to positron-atom virtual states [3,36,61]. However, the absolute values obtained are still about five times lower than the benchmark.

The remaining 80% come from the nonlocal corrections to the annihilation vertex, diagrams (b)–(f) in Fig. 5. The contributions of all the diagrams evaluated using the positron Dyson orbitals and the total Z_{eff} are shown in Fig. 11 for the positron s, p, and d partial waves.

The difficulty of calculating the vertex corrections to Z_{eff} accurately is evident from these graphs, as all the diagrams in Fig. 5 contribute significantly. The higher-order diagrams containing the vertex function, are close to or greater than the lower-order diagrams. Note that all contributions have a similar dependence on the positron momentum. It is driven by the momentum dependence of the positron Dyson orbitals (external lines in the diagrams), as discussed in Sec. II D.

Figure 11 shows that for p and d waves, the contribution of the diagram Fig. 5(f) grows rapidly and becomes largest towards the Ps formation threshold. This diagram describes annihilation inside the virtual Ps formation, which has a vig-
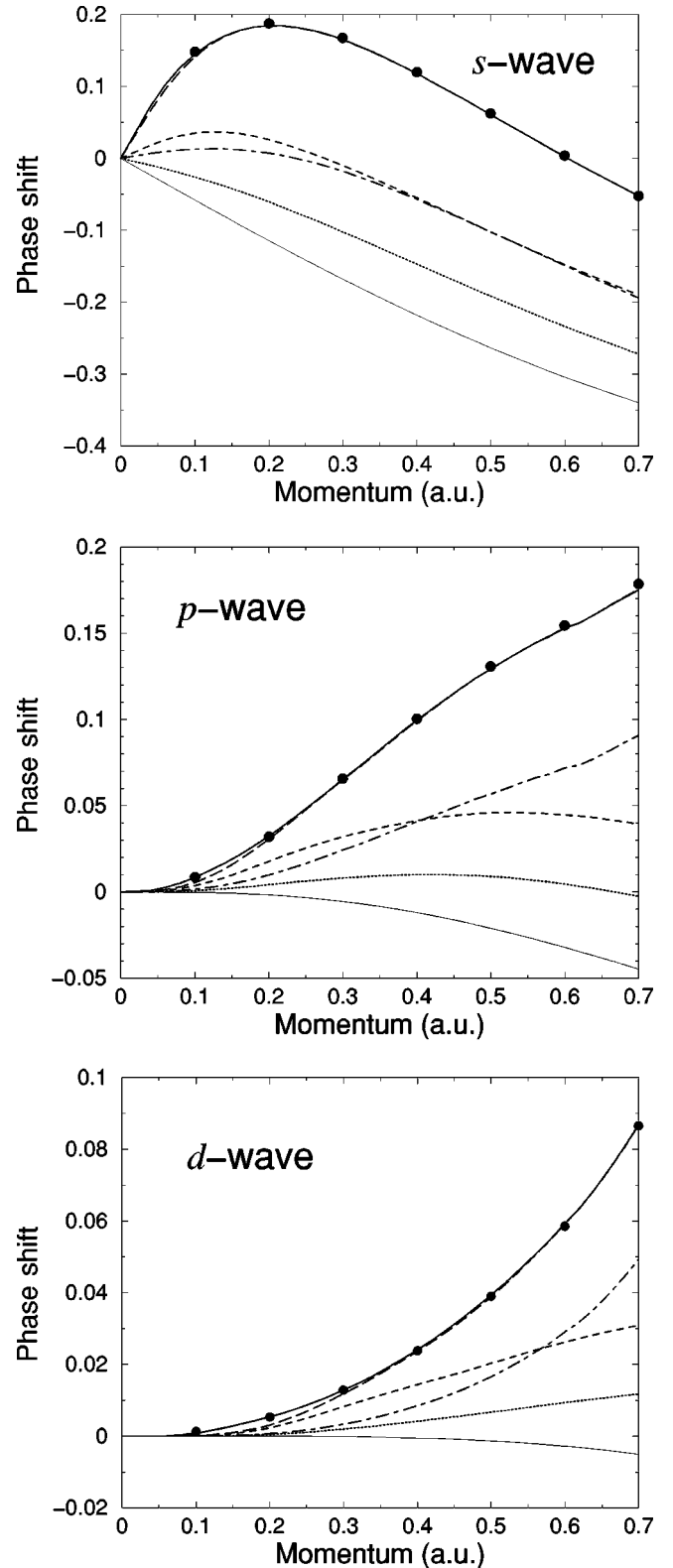

FIG. 9. Positron-hydrogen s-, p-, and d-wave scattering phase shifts: long-dashed curve, many-body theory ($R=15$ a.u.); solid curve, many-body theory ($R=30$ a.u.); circles, variational calculation [13]. Thin solid curve, static approximation; dashed curve, $\Sigma^{(2)}$; dotted-dashed curve, $\Sigma^{(\Gamma)}$; dotted curve, $\Sigma^{(\Gamma)}$ obtained with $\Gamma=V$ (all $R=15$).

TABLE II. Comparison of many-body phase shifts and Z_{eff} with those from an accurate variational calculation.

k (a.u.)	Phase shifts						Z_{eff}					
	s wave		p wave		d wave		s wave		p wave		d wave	
	MB[a]	Var[b]	MB	Var	MB	Var	MB	Var	MB	Var	MB	Var
0.1	0.1447	0.1479	0.0084	0.0086	0.0008	0.0013	6.7806	7.5679	0.1227	0.1422	0.0008	0.0010
0.2	0.1842	0.1875	0.0320	0.0320	0.0054	0.0053	5.1058	5.7619	0.4842	0.5461	0.0128	0.0150
0.3	0.1654	0.1672	0.0653	0.0657	0.0129	0.0128	3.9289	4.3515	1.0218	1.1375	0.0615	0.0704
0.4	0.1180	0.1198	0.0996	0.1003	0.0241	0.0238	3.1119	3.4073	1.6067	1.7940	0.1773	0.2009
0.5	0.0605	0.0624	0.1290	0.1306	0.0393	0.0390	2.5459	2.7470	2.1349	2.4015	0.3889	0.4399
0.6	0.0024	0.0036	0.1529	0.1544	0.0593	0.0585	2.1449	2.2848	2.6312	2.9457	0.7512	0.8346
0.7	−0.0524	−0.0523	0.1750	0.1786	0.0867	0.0866	1.8401	1.9719	3.3140	3.9278	1.4480	1.6756

[a]Present calculation for $R=15$ a.u.
[b]Kohn variational calculations, Refs. [13,60].

orous energy dependence close to threshold [51]. This may have a bearing on the kinks in Z_{eff} visible at $k \approx 0.6$ a.u. for the p and d waves. Although they may be a numerical artifact, an indication of an inflection point is also present in the accurate p-wave results of Ref. [60].

The total Z_{eff} values obtained for $R=15$ a.u. are slightly higher than those for $R=30$ a.u. A denser knot sequence for $R=15$ provides a better description of small electron-positron separations. Our final results compare well with those from the accurate variational calculation, Ref. [60] (see Table II), although they are systematically lower. In Ref. [60] and *all* other calculations of positron-hydrogen annihilation (see, e.g., Ref. [62]), the electron-positron distance is represented explicitly in the calculation, while we use a single-center expansion. The discrepancy is therefore related to the difficulty in describing small electron-positron separations. We believe that it could be eliminated by "pushing harder" the numerics in our approach. Thus Fig. 11 (*s* wave) shows that
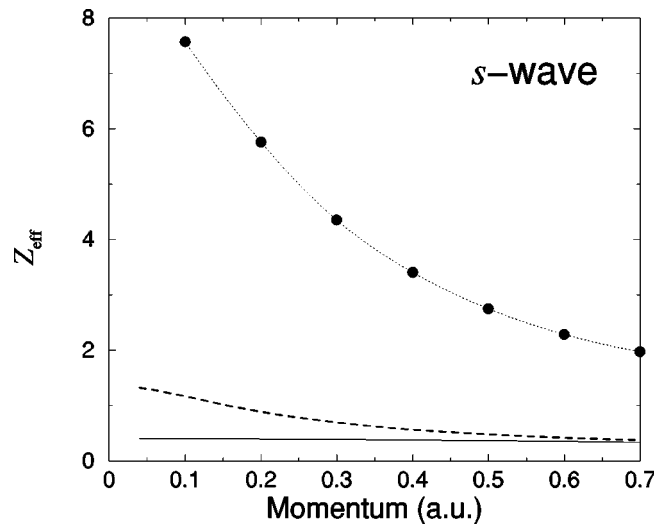

FIG. 10. Contribution of the zeroth-order diagram, Fig. 5(a), to the positron-hydrogen *s*-wave annihilation parameter Z_{eff}, calculated with the positron wave function in the static atomic potential (solid curve), and with the Dyson orbital (dashed curve). Circles connected by dotted curve are the accurate results of Ref. [60].

when we use $n=60$ B splines of order $k=9$ and include the first 23 basis states, the difference between our Z_{eff} and the benchmark values is halved. However, using larger n would require the inclusion of more basis states, which would lead to impractically large sizes of the vertex function matrix.

The main conclusion of this section is that the numerical implementation of the many-body theory approach proposed in this paper works. For positron collisions with hydrogen, where this approach is exact, the calculations reproduce the best scattering phase shifts, and yield good results in the more difficult annihilation problem.

V. CORRELATION CONTRIBUTION TO THE ANNIHILATION VERTEX

The ability of a many-body theory to describe correlation corrections to the annihilation vertex may give some insight into their role in positron annihilation with matter. Thus in theoretical studies of positron annihilation in condensed-matter systems the annihilation rate is often found in the form (see, e.g., Ref. [6]),

$$\lambda = \pi r_0^2 c \int \rho_e(\mathbf{r}) \rho_p(\mathbf{r}) \gamma(\rho_e, \rho_p) d\mathbf{r}, \qquad (37)$$

where $\rho_e(\mathbf{r})$ and $\rho_p(\mathbf{r})$ are the electron and positron densities and $\gamma(\rho_e, \rho_p)$ is the *enhancement factor* introduced to account for the Coulomb attraction in the annihilating pair. It has long been known that the independent-particle approximation ($\gamma=1$) underestimates the annihilation rates by several times [63], and a number of semiempirical and interpolation forms of $\gamma(\rho_e, \rho_p)$ have been suggested (see, e.g., Ref. [64] and references therein).

A comparison between Eq. (37) with $\gamma=1$ and the many-body theory expression (24) shows that the former corresponds to the zeroth-order term in Z_{eff}, Eq. (22) [65]. As we have seen in Sec. IV (Fig. 10), $Z_{eff}^{(0)}$ does underestimate the annihilation rate in hydrogen by a factor of 5, even when the best positron wave function is used. The correlation correction to the annihilation rate [second term in Eq. (24)] does not have the form of Eq. (37). It depends on the positron wave function at two different points, $\mathbf{r}$ and $\mathbf{r}'$, hence any
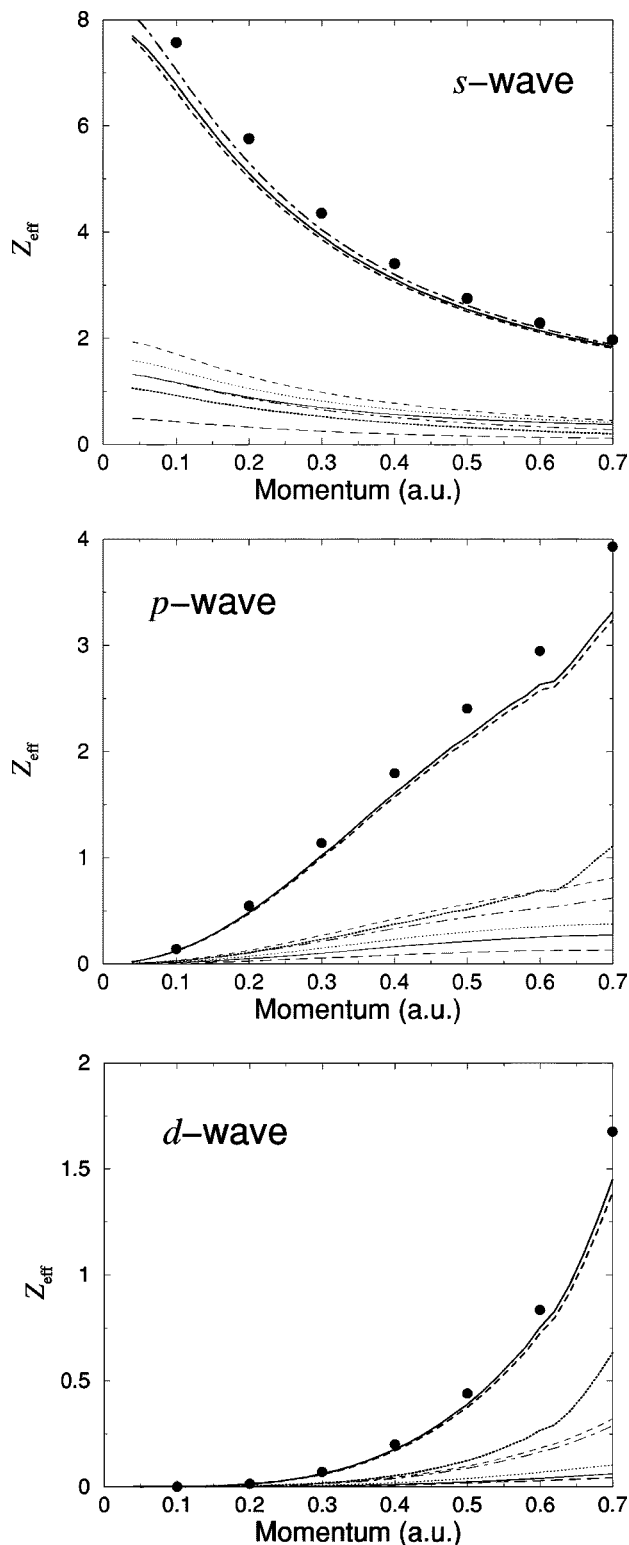
FIG. 11. Annihilation parameter Z_{eff} for the s-, p-, and d-wave positron on hydrogen. Contributions of individual diagrams from Fig. 5 are: solid curve, diagram (a); dotted curve, (b); long-dashed curve, (c); dashed curve, (d); dotted-dashed curve, (e); thick dotted curve, (f) (all for $R=15$ a.u.). Thick solid curve is the total for $R=15$ a.u., thick dashed curve, total for $R=30$ a.u.; thick dotted-dashed curve (s-wave), a calculation for $R=30$ a.u. with 23 out of $n=60$ ninth-order B splines. Circles are the results of Ref. [60].
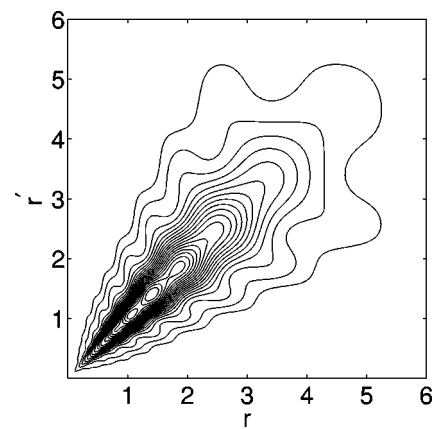

FIG. 12. Radial dependence of the integrand (38) of the correlation correction for the annihilation of the s-wave positron with momentum $k=0.06$ a.u. on hydrogen. The "ripples" is an artifact of the reconstruction of $\Delta_\varepsilon^{(l)}(r,r')$ from the matrix element $\langle i|\Delta_\varepsilon|j\rangle$.

local expression like Eq. (37) is necessarily an approximation.

To illustrate this point, a contour plot in Fig. 12 shows the radial part of the integrand of the nonlocal term,

$$P_{\varepsilon l}(r)\Delta_\varepsilon^{(l)}(r,r')P_{\varepsilon l}(r'), \qquad (38)$$

for the s-wave ($l=0$) positron annihilation on hydrogen at $k=0.06$ a.u. The plot confirms that the correlation contribution to the annihilation vertex is localized near the atom. Its maximum at $r=r'\approx 1.5$ a.u. compares well with the radius of the hydrogen atom, and the ridgelike structure indicates that the "nonlocality" is limited to $|r-r'|\sim 1$ a.u.

The overall size of the (nonlocal) correction to the annihilation vertex can be characterized by the average enhancement factor,

$$\bar{\gamma} = 1 + \frac{\int \psi_\varepsilon^*(\mathbf{r})\Delta_\varepsilon(\mathbf{r},\mathbf{r}')\psi_\varepsilon(\mathbf{r}')d\mathbf{r}d\mathbf{r}'}{\int \sum_n |\varphi_n(\mathbf{r})|^2 |\psi_\varepsilon(\mathbf{r})|^2 d\mathbf{r}}. \qquad (39)$$

We define this factor in such a way that when used in place of γ in Eq. (37), together with $\rho_e(\mathbf{r})=\Sigma_n|\varphi_n(\mathbf{r})|^2$ and $\rho_p(\mathbf{r})=|\psi_\varepsilon(\mathbf{r})|^2$, it would reproduce correct values of the positron-atom annihilation rate.

The quantity $\bar{\gamma}$ can also be defined as the ratio of the total Z_{eff} to the value obtained from the zeroth-order diagram $Z_{\text{eff}}^{(0)}$, Fig. 5(a). Since large energies of the intermediate virtual states dominate Δ_ε (see Sec. II D), this ratio should depend weakly on the energy of the incident positron, or the type of the wave function of the incident positron. In particular, the use of either HF or Dyson wave functions ψ_ε for the incident positron should yield similar values of $\bar{\gamma}$.

This understanding is confirmed by Fig. 13, which shows $\bar{\gamma}$ for the s-, p-, and d-wave positrons on hydrogen. The values of $\bar{\gamma}$ depend weakly on the positron energy, except when the Ps formation threshold is approached. This agrees with the earlier observation that the energy dependence of various contributions to Z_{eff} in Fig. 11 is approximately the
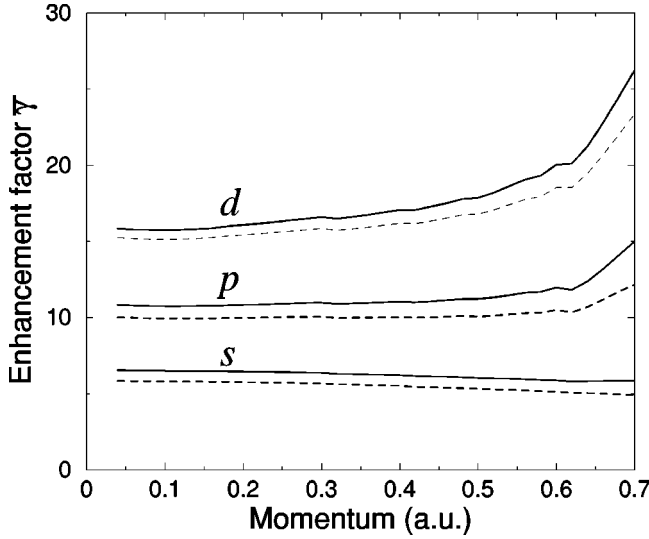
FIG. 13. Ratio $\bar{\gamma}$ of the total Z_{eff} to $Z_{\text{eff}}^{(0)}$ for positron annihilation on hydrogen. Values obtained with positron wave function in the static approximation are shown by solid curves, and those with the Dyson orbitals, by dashed curves.

FIG. 14. Effective electron correlation densities $\tilde{\rho}_e^{[1]}(r)$ (dashed curve) and $\tilde{\rho}_e^{[2]}(r)$ (dotted-dashed curve) for the annihilation of the s-wave positron with $k=0.5$ on hydrogen. Shown for comparison are the ground-state electron density in hydrogen $\rho_e(r)$ (solid curve), and the positron density $P_{\varepsilon l}^2(r)$ (dotted curve, arbitrarily scaled).

same. The values of $\bar{\gamma}$ obtained with the static and Dyson orbitals are close to each other, even though the absolute values of Z_{eff} obtained in the two approximations are very different (see, e.g., Fig. 10). On the other hand, the enhancement factor increases with the positron angular momentum. For larger l, the penetration of the positron into the electron-rich regions of the atom is suppressed by the centrifugal barrier, and the effect of "pulling the electron out" (i.e., virtual Ps formation), described by the correlation corrections, becomes more important.

In order to compare the enhancement of Z_{eff} due to the nonlocal vertex correction term with the local enhancement factors used in condensed-matter calculations, we need to "localize" the contribution of $\Delta_\varepsilon(\mathbf{r}, \mathbf{r}')$. We do this by introducing an effective "electron correlation density" $\tilde{\rho}_e(r)$ via the relation

$$\int\int P_{\varepsilon l}(r)\Delta_\varepsilon^{(l)}(r,r')P_{\varepsilon l}(r')drdr' \equiv \int \tilde{\rho}_e(r)P_{\varepsilon l}^2(r)dr,$$
(40)

for positron annihilation in the lth partial wave. This allows us to define an effective enhancement factor $\gamma_e(r)$ through

$$\rho_e(r) + \tilde{\rho}_e(r) \equiv \gamma_e(r)\rho_e(r),$$
(41)

where $\rho_e(r) = P_{1s}^2(r)/4\pi r^2$, and $P_{1s}=2re^{-r}$ for hydrogen. Equations (40) and (41) guarantee that when we use $\gamma_e(r)$ in Eq. (37), correct annihilation rates are recovered.

Equation (40) does not define $\tilde{\rho}_e(r)$ uniquely. We use two different methods to obtain it numerically. The first one states
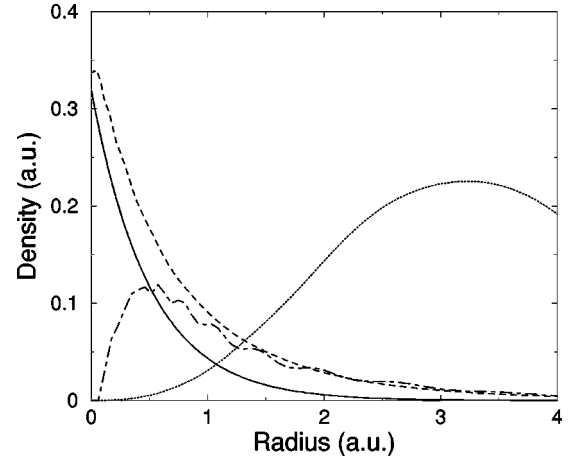
$$\tilde{\rho}_e^{[1]}(r) = \frac{\int \Delta_\varepsilon^{(l)}(r,r')P_{\varepsilon l}(r')dr'}{P_{\varepsilon l}(r)}$$
(42)

which ensures that $\tilde{\rho}_e^{[1]}(r)$ satisfies Eq. (40) exactly. However, it has a disadvantage in that it may have unphysical poles at the zeroes of the positron wave function. A second method involves calculating

$$\tilde{\rho}_e^{[2]}(r) = \int_{-2r}^{2r} \Delta_\varepsilon^{(l)}(r+\sigma/2,r-\sigma/2)d\sigma,$$
(43)

which follows from Eq. (40) if we change variables r, r' to $r\pm\sigma/2$, and keep the lowest-order term in the Taylor expansion of $P_{\varepsilon l}(r+\sigma/2)P_{\varepsilon l}(r-\sigma/2)$. This approximation may not be accurate for small r, where the positron wave function varies rapidly, but should be correct for larger r values, where the peaking of $\Delta_\varepsilon^{(l)}(r,r')$ at $r=r'$ (Fig. 12) means that $P_{\varepsilon l}(r)$ varies slowly on the scale of typical σ.

Figure 14 shows both electron correlation densities calculated for the s-wave positron with momentum $k=0.5$ a.u. Apart from the small range of distances near the origin, the values of $\tilde{\rho}_e$ from the two methods are close, although $\tilde{\rho}_e^{[2]}$ shows some numerical "noise" related to the reconstruction of $\Delta_\varepsilon^{(l)}(r,r')$ from its matrix elements. A comparison with the hydrogen ground-state electron density shows that the latter drops much faster with the distance from the nucleus. In fact, $\tilde{\rho}_e$ is much greater than ρ_e at those r where the positron density is large, in agreement with the correlation contribution to Z_{eff} being five times $Z_{\text{eff}}^{(0)}$.

In Fig. 15 the enhancement factor obtained from $\tilde{\rho}_e^{[1]}$ is compared with a commonly used parametrization of $\gamma(\rho_e, \rho_p)$ derived by Arponen and Pajanne [66] for a positron in a homogeneous electron gas,
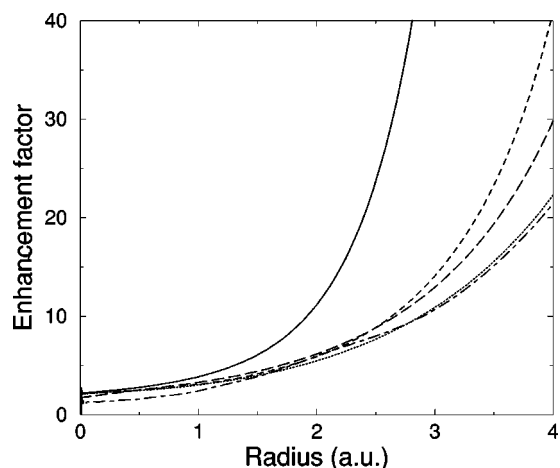
FIG. 15. Enhancement factors for positron annihilation on hydrogen. Solid curve, γ_{AP}, Eq. (44); dotted line γ_e for s-wave positrons at $k=0.06$; dashed line, γ_e for s-wave positrons at $k=0.5$; long-dashed line, γ_e for p-wave positrons at $k=0.5$; dotted-dashed line, γ_e for d-wave positrons at $k=0.5$.

$$\gamma_{AP} = 1 + 1.23 r_s - 0.0742 r_s^2 + \tfrac{1}{6} r_s^3, \qquad (44)$$

where r_s is a measure of the average distance between the electrons,

$$r_s = \left(\frac{3}{4\pi\rho_e} \right)^{1/3}. \qquad (45)$$

Unlike γ_{AP}, the factor γ_e obtained from our many-body theory approach, depends on the energy and orbital angular momentum of the positron. The values shown in Fig. 15 correspond to the momenta $k=0.06$ (s wave) and 0.5 a.u. (s, p, and d waves).

A feature common to all enhancement factors in Fig. 15 is their rapid rise with the distance from the nucleus. This increase is related to the drop of the electron density, a relation which is explicit in Eq. (44) for γ_{AP}. At small distances, where the electron density is large, γ_{AP} compares well with γ_e. However, at larger distances, where the electron density is low, γ_{AP} is much greater than all of the γ_e. Such a discrepancy could be expected, given that a homogeneous electron gas theory used to derive γ_{AP} is more reliable in the high-density limit. The exaggeration of the enhancement by γ_{AP} was reported in Ref. [64] where various forms of the enhancement factor were tested by comparison with accurate annihilation rates for a number of positron-atom bound systems. For Be and Mg (which have $I>6.8$ eV), the values obtained using γ_{AP} overestimated the accurate annihilation rates by factors of 5 and 2, respectively. Note also that the product $\rho_e \gamma_{AP}$ remains finite as $\rho_e \rightarrow 0$. This means that one cannot in principle use it in Eq. (37) for a continuous spectrum positron, since it would yield infinite values of the annihilation rate and Z_{eff}. For the same reason a much stronger overestimate observed in Ref. [64] with γ_{AP} for Be is a direct consequence of the positron binding energy for Be being much smaller than for Mg.

Figure 15 shows that the values of γ_e derived for the p and d waves are similar to those from the s wave. Hence the large differences between the average enhancement factors in Fig. 13 are due to the effect of the centrifugal barrier on the positron wave function. The distances which effectively contribute to Z_{eff} are greater for the positron in higher partial waves.

VI. SUMMARY AND OUTLOOK

In this paper we have formulated a many-body theory approach which accounts for the main correlation effects in positron-atom interactions. These are (i) polarization of the target by the positron, (ii) virtual positronium formation, and (iii) strong enhancement of the electron-positron contact density due to their Coulomb interaction. The key development for an accurate description of (ii) and (iii) is the summation of the ladder diagram series and calculation of the electron-positron vertex function. B-spline basis sets and extrapolation over the orbital angular momenta are used to achieve convergence of the sums over the electron and positron intermediate states. The method can be applied to a range of problems such as positron scattering, annihilation, and formation of bound states. A many-body diagrammatic approach can also be developed to calculate the angular correlation between the annihilation γ quanta, or the spectrum of the gamma rays [67].

Although our main interest is in exploring many-electron targets, the method has been first tested for hydrogen, where accurate benchmark data exist for the scattering phase shifts and annihilation rates. In the case of hydrogen the present formalism is exact. Numerically, excellent agreement with accurate variational calculations for the phase shifts has been obtained, together with a good agreement for the annihilation parameter Z_{eff}. The calculation of the most difficult part of the correlation potential, which contains the vertex function, for many-electron atoms is only marginally more difficult than for hydrogen. Therefore we expect that application of our many-body theory to the problems of positron scattering and annihilation on noble-gas atoms and binding to halogen ions [68,69] should yield accurate results. In particular, we would like to re-examine and improve the accuracy of the many-body theory predictions [35] of positron binding energies to the ns^2 atoms such as Mg, Cd, and Zn.

The advantage of many-body theory methods is their physical transparency. It allows one to distinguish between different physical mechanisms and compare their relative importance. Thus we saw that virtual Ps formation in positron-hydrogen scattering is just as important as the target polarization. Correlation corrections to the annihilation vertex, which are physically related to the virtual Ps formation, are even more important. They enhance the annihilation rate in hydrogen by a factor of 5 or more, depending on the positron partial wave. Such vertex corrections depend weakly on the positron energy, and the enhancement they produce is practically the same for various positron wave functions. Therefore one could use the average enhancement factors derived for isolated atoms to obtain reliable annihilation rates for atoms placed in different environments, provided that a sufficiently accurate single-particle positron wave function is available. Of course, different atomic subshells will be char-

acterized by different enhancement factors. However, they can all be determined in many-body calculations of the type described in this paper, and serve as an input for the calculations of positron annihilation in molecules or condensed matter.

In this work we have analyzed the spatial dependence of the nonlocal correlation corrections to the annihilation vertex. We have also derived the equivalent local enhancement factor and compared it with an expression used in condensed-matter calculations. Similar comparisons for larger many-electron targets may test various forms of enhancement factors in a much greater range of electron densities.

The rapid development of computers over the past few decades seems to have favored theoretical methods other than the many-body theory. Such methods often rely more on the computer power and numerical techniques than on the physical insight. They often appear to be "more exact" than the sophisticated but explicitly approximate many-body theory approaches, and promise improved results due to shear growth of computer power. Their drawback is that they do not always increase one's physical understanding of the problem. We believe that a further theoretical development of many-body methods combined with a judicial use of computers is a healthy alternative.

ACKNOWLEDGMENTS

APPENDIX: MATRIX ELEMENTS AND DIAGRAMS

For a positron interacting with a spherically symmetric target, the self-energy $\Sigma_E(\mathbf{r}, \mathbf{r}')$ and the correlation correction to the annihilation vertex $\Delta_E(\mathbf{r}, \mathbf{r}')$ can be expanded in partial waves, e.g.,

$$\Sigma_E(\mathbf{r}, \mathbf{r}') = \frac{1}{rr'} \sum_{\lambda=0}^{\infty} \sum_{\mu=-\lambda}^{\mu=\lambda} Y_{\lambda\mu}(\Omega) \Sigma_E^{(\lambda)}(r,r') Y_{\lambda\mu}^*(\Omega').$$

(A1)

Defining the volume element $d\mathbf{r} = r^2 dr d\Omega$, and the positron wave function with orbital angular momentum l, $\varphi_\varepsilon(\mathbf{r}) = r^{-1} P_{\varepsilon l}(r) Y_{lm}(\Omega)$, we obtain the matrix element $\langle \varepsilon | \Sigma | \varepsilon' \rangle$ as

$$\langle \varepsilon | \Sigma_E | \varepsilon' \rangle = \int \varphi_\varepsilon^*(\mathbf{r}) \Sigma_E(\mathbf{r}, \mathbf{r}') \varphi_{\varepsilon'}(\mathbf{r}') d\mathbf{r}$$

$$= \int P_{\varepsilon l}(r) \Sigma_E^{(l)}(r,r') P_{\varepsilon' l}(r') dr dr'. \quad \text{(A2)}$$

The angular reduction of the various diagrams in $\langle \varepsilon | \Sigma_E | \varepsilon' \rangle$

and $\langle \varepsilon | \Delta_E | \varepsilon \rangle$ is simplified by the use of graphical techniques for performing angular momentum algebra [70].

The reduced Coulomb matrix element is defined as

$$\langle 3,4 \| V_l \| 2,1 \rangle = \sqrt{[l_1][l_2][l_3][l_4]} \begin{pmatrix} l_1 & l & l_3 \\ 0 & 0 & 0 \end{pmatrix} \begin{pmatrix} l_2 & l & l_4 \\ 0 & 0 & 0 \end{pmatrix}$$

$$\times \int P_{\varepsilon_3 l_3}(r_1) P_{\varepsilon_4 l_4}(r_2) \frac{r_<^l}{r_>^{l+1}}$$

$$\times P_{\varepsilon_2 l_2}(r_2) P_{\varepsilon_1 l_1}(r_1) dr_1 dr_2, \quad \text{(A3)}$$

where $[l_1] \equiv 2l_1 + 1$, etc. The minus sign in the reduced Coulomb matrix element involving the positron is accounted for in the overall sign factor for the diagram (see below). The reduced Coulomb matrix element for an electron-positron pair coupled into a total angular momentum J is given by

$$\langle 3,4 \| V^{(J)} \| 2,1 \rangle = \sum_l (-1)^{J+l} \langle 3,4 \| V_l \| 2,1 \rangle \begin{Bmatrix} J & l_3 & l_4 \\ l & l_2 & l_1 \end{Bmatrix}.$$

(A4)

This expression is similar to the "exchange" matrix element that one meets in all-electron problems [22].

The sum of the ladder diagram series (the vertex function) is calculated via the matrix equation (6) solved for all possible total angular momenta J of the electron-positron pair:

$$\langle \nu_2, \mu_2 \| \Gamma_E^{(J)} \| \mu_1, \nu_1 \rangle = -\langle \nu_2, \mu_2 \| V^{(J)} \| \mu_1, \nu_1 \rangle$$

$$- \sum_{\nu,\mu} \frac{\langle \nu_2, \mu_2 \| V^{(J)} \| \mu, \nu \rangle \langle \nu, \mu \| \Gamma_E^{(J)} \| \mu_1, \nu_1 \rangle}{E - \varepsilon_\nu - \varepsilon_\mu}.$$

(A5)

In the Appendix, the state labels ν, ν_1, etc., refer to the positron orbitals $\varepsilon_\nu l_\nu$, $\varepsilon_{\nu_1} l_{\nu_1}$, etc. Similarly, μ, μ_1, etc., label excited-state electron orbitals. Electron orbitals occupied in the target ground state (holes) are labeled by Latin indices (n). When B-spline basis states are used, Eq. (A5) is a finite-dimension linear equation solved by standard methods.

For closed-shell atoms, each loop in the diagram gives a spin factor of 2. This factor should be omitted for hydrogen which has only one electron in the $1s$ orbital. The sign factor for each diagram is $(-1)^{a+b+c}$, where a is the number of hole lines, b is the number of electron-hole loops, and c is the number of positron-electron Coulomb interactions. In the expressions below ε and ε' are the external positron lines, and the angular momentum of the incident positron is l_p.

The second-order self-energy diagram, Fig. 1(a), is given by

$$2 \sum_{\nu,\mu,n} \sum_l \frac{\langle \varepsilon', n \| V_l \| \mu, \nu \rangle \langle \nu, \mu \| V_l \| n, \varepsilon \rangle}{[l][l_p](E + \varepsilon_n - \varepsilon_\nu - \varepsilon_\mu)}. \quad \text{(A6)}$$

The virtual-Ps contribution to Σ_E, Fig. 2, is obtained after finding the vertex function as follows:

$$2 \sum_{\nu_i,\mu_i,n} \sum_J \frac{[J]\langle \varepsilon',n\|V^{(J)}\|\mu_2,\nu_2\rangle\langle \nu_2,\mu_2\|\Gamma^{(J)}_{E+\varepsilon_n}\|\mu_1,\nu_1\rangle\langle \nu_1,\mu_1\|V^{(J)}\|n,\varepsilon\rangle}{[l_p](E+\varepsilon_n-\varepsilon_{\nu_1}-\varepsilon_{\mu_1})(E+\varepsilon_n-\varepsilon_{\nu_2}-\varepsilon_{\mu_2})}. \tag{A7}$$

Matrix elements of the annihilation δ function are defined similarly to the Coulomb ones, using the expansion of the $\delta(\mathbf{r}_1-\mathbf{r}_2)$ in terms of spherical harmonics [70]. The reduced matrix element then is

$$\langle 3,4\|\delta_l\|2,1\rangle = \frac{[l]}{4\pi}\sqrt{[l_1][l_2][l_3][l_4]}\begin{pmatrix} l_1 & l & l_3 \\ 0 & 0 & 0 \end{pmatrix}\begin{pmatrix} l_2 & l & l_4 \\ 0 & 0 & 0 \end{pmatrix}$$

$$\times \int P_{\varepsilon_3 l_3}(r)P_{\varepsilon_4 l_4}(r)P_{\varepsilon_2 l_2}(r)P_{\varepsilon_1 l_1}(r)r^{-2}dr, \tag{A8}$$

and the matrix element for an electron-positron pair coupled into a total angular momentum J is given by

$$\langle 3,4\|\delta^{(J)}\|2,1\rangle = \sum_l (-1)^{J+l}\langle 3,4\|\delta_l\|2,1\rangle \begin{Bmatrix} J & l_3 & l_4 \\ l & l_2 & l_1 \end{Bmatrix}. \tag{A9}$$

The diagrams contributing to Z_{eff} also contain factors of 2 for each closed loop, which must be removed for hydrogen. In the diagrams below, we also include factors of 2 to account for the mirror images of those diagrams that are not symmetric. To produce correct values of Z_{eff} the expressions given below must be multiplied by the normalization factor (25).

The zeroth-order diagram, Fig. 4(a), is a sum of simple radial integrals over all hole orbitals n,

$$2\sum_n \frac{[l_n]}{4\pi}\int P^2_{\varepsilon l_p}(r)P^2_{\varepsilon_n l_n}(r)r^{-2}dr. \tag{A10}$$

The first-order contribution, Figs. 4(b) and 4(c), is given by

$$-4\sum_{\nu,\mu,n}\sum_l \frac{\langle \varepsilon,n\|\delta_l\|\mu,\nu\rangle\langle \nu,\mu\|V_l\|n,\varepsilon\rangle}{[l][l_p](E+\varepsilon_n-\varepsilon_\nu-\varepsilon_\mu)}. \tag{A11}$$

Expressions for the remaining four contributions, Figs. 5(c)–5(f), are

$$2\sum_{\nu_i,\mu_i,n}\sum_J \frac{[J]\langle \varepsilon,n\|V^{(J)}\|\mu_2,\nu_2\rangle\langle \nu_2,\mu_2\|\delta^{(J)}\|\mu_1,\nu_1\rangle\langle \nu_1,\mu_1\|V^{(J)}\|n,\varepsilon\rangle}{[l_p](E+\varepsilon_n-\varepsilon_{\nu_2}-\varepsilon_{\mu_2})(E+\varepsilon_n-\varepsilon_{\nu_1}-\varepsilon_{\mu_1})}, \tag{A12}$$

$$-4\sum_{\nu_i,\mu_i,n}\sum_J \frac{[J]\langle \varepsilon,n\|\delta^{(J)}\|\mu_2,\nu_2\rangle\langle \nu_2,\mu_2\|A^{(J)}_{E+\varepsilon_n}\|n,\varepsilon\rangle}{[l_p](E+\varepsilon_n-\varepsilon_{\nu_2}-\varepsilon_{\mu_2})}, \tag{A13}$$

$$4\sum_{\nu_i,\mu_i,n}\sum_J \frac{[J]\langle \varepsilon,n\|V^{(J)}\|\mu_3,\nu_3\rangle\langle \nu_3,\mu_3\|\delta^{(J)}\|\mu_2,\nu_2\rangle\langle \nu_2,\mu_2\|A^{(J)}_{E+\varepsilon_n}\|n,\varepsilon\rangle}{[l_p](E+\varepsilon_n-\varepsilon_{\nu_3}-\varepsilon_{\mu_3})(E+\varepsilon_n-\varepsilon_{\nu_2}-\varepsilon_{\mu_2})}, \tag{A14}$$

$$2\sum_{\nu_i,\mu_i,n}\sum_J \frac{[J]\langle \varepsilon,n\|A^{(J)}_{E+\varepsilon_n}\|\mu_3,\nu_3\rangle\langle \nu_3,\mu_3\|\delta^{(J)}\|\mu_2,\nu_2\rangle\langle \nu_2,\mu_2\|A^{(J)}_{E+\varepsilon_n}\|n,\varepsilon\rangle}{[l_p](E+\varepsilon_n-\varepsilon_{\nu_3}-\varepsilon_{\mu_3})(E+\varepsilon_n-\varepsilon_{\nu_2}-\varepsilon_{\mu_2})}, \tag{A15}$$

where we have introduced

$$\langle \nu_2,\mu_2\|A^{(J)}_{E+\varepsilon_n}\|n,\varepsilon\rangle = \sum_{\nu_1,\mu_1} \frac{\langle \nu_2,\mu_2\|\Gamma^{(J)}_{E+\varepsilon_n}\|\mu_1,\nu_1\rangle\langle \nu_1,\mu_1\|V^{(J)}\|n,\varepsilon\rangle}{E+\varepsilon_n-\varepsilon_{\nu_1}-\varepsilon_{\mu_1}}. \tag{A16}$$

[1] W. J. Cody, J. Lawson, H. S. W. Massey, and K. Smith, Proc. R. Soc. London, Ser. A **278**, 479 (1964).

[2] M. Ya. Amusia, N. A. Cherepkov, L. V. Chernysheva, and S. G. Shapiro, J. Phys. B **9**, L531 (1976).

[3] V. A. Dzuba, V. V. Flambaum, W. A. King, B. N. Miller, and O. P. Sushkov, Phys. Scr. **T46**, 248 (1993).

[4] G. F. Gribakin and W. A. King, J. Phys. B **27**, 2639 (1994).

[5] *New Directions in Antimatter Chemistry and Physics*, edited

by C. M. Surko and F. A. Gianturco (Kluwer Academic Publishers, Dordrecht, 2001).

[6] M. J. Puska and R. M. Nieminen, Rev. Mod. Phys. **66**, 841 (1994).

[7] A. David, G. Kögel, P. Sperr, and W. Triftshäuser, Phys. Rev. Lett. **87**, 067402 (2001).

[8] G. Jerusalem, R. Hustinx, Y. Beguin, and G. Fillet, Eur. J. Cancer **39**, 1525 (2003).

[9] C. Schwartz, Phys. Rev. **124**, 1468 (1961).

[10] A. K. Bhatia, A. Temkin, R. J. Drachman, and H. Eiserike, Phys. Rev. A **3**, 1328 (1971); A. K. Bhatia, A. Temkin, and H. Eiserike, *ibid.* **9**, 219 (1974).

[11] J. W. Humberston, J. Phys. B **6**, L305 (1973); R. I. Campeanu and J. W. Humberston, *ibid.* **10**, L153 (1977).

[12] J. W. Humberston, Adv. At. Mol. Phys. **15**, 101 (1979).

[13] J. W. Humberston, P. Van Reeth, M. S. T. Watts, and W. E. Meyerhof, J. Phys. B **30**, 2477 (1997).

[14] P. Van Reeth and J. W. Humberston, J. Phys. B **32**, 3651 (1999).

[15] M. T. McAlinden, A. A. Kernoghan, and H. R. J. Walters, Hyperfine Interact. **89**, 161 (1994); J. Phys. B **29**, 555 (1996); **29**, 3971 (1996); **30**, 1543 (1997).

[16] G. G. Ryzhikh, J. Mitroy, and K. Varga, J. Phys. B **31**, 3965 (1998).

[17] V. A. Dzuba, V. V. Flambaum, G. F. Gribakin, and C. Harabati, Phys. Rev. A **60**, 3641 (1999); V. A. Dzuba, V. V. Flambaum, and C. Harabati, *ibid.* **62**, 042504 (2000).

[18] I. A. Ivanov, J. Mitroy, and K. Varga, Phys. Rev. Lett. **87**, 063201 (2001); J. Mitroy and I. A. Ivanov, Phys. Rev. A **65**, 012509 (2002).

[19] M. W. J. Bromley and J. Mitroy, Phys. Rev. A **65**, 062505 (2002); **65**, 062506 (2002).

[20] M. W. J. Bromley and J. Mitroy, Phys. Rev. A **66**, 062504 (2002); **67**, 062709 (2003).

[21] A. L. Fetter and J. D. Walecka, *Quantum Theory of Many-Particle Systems* (McGraw-Hill, New York, 1971).

[22] M. Ya. Amusia and N. A. Cherepkov, Case Stud. At. Phys. **5**, 47 (1975).

[23] *Many-body Theory of Atomic Structure and Photoionization*, edited by T. N. Chang (World Scientific, Singapore, 1993).

[24] H. P. Kelly, Phys. Rev. **131**, 684 (1963).

[25] M. Ya. Amusia, N. A. Cherepkov, L. V. Chernysheva, S. G. Shapiro, and A. Tanchich, Pis'ma Zh. Eksp. Teor. Fiz. **68**, 2023 (1975); [Sov. Phys. JETP **41**, 1012 (1975)].

[26] M. Ya. Amusia, N. A. Cherepkov, L. V. Chernysheva, D. M. Davidović, and V. Radojević, Phys. Rev. A **25**, 219 (1982). According to this paper the coefficient in Eq. (15) is $-\pi$, because they express the self-energy operator Σ_E in Rydberg.

[27] W. R. Johnson and C. Guet, Phys. Rev. A **49**, 1041 (1994); **64**, 019901 (2001).

[28] *Many-body Atomic Physics*, edited by J. J. Boyle and M. S. Pindzola (Cambridge University Press, Cambridge, England, 1995).

[29] L. V. Chernysheva, G. F. Gribakin, V. K. Ivanov, and M. Yu. Kuchiev, J. Phys. B **21**, L419 (1988); G. F. Gribakin, B. V. Gultsev, V. K. Ivanov, and M. Yu. Kuchiev, J. Phys. B **23**, 4505 (1990).

[30] W. R. Johnson, J. Sapirstein, and S. A. Blundell, J. Phys. B **22**, 2341 (1989).

[31] V. A. Dzuba, V. V. Flambaum, G. F. Gribakin, and O. P. Sushkov, Phys. Rev. A **44**, 2823 (1991).

[32] V. A. Dzuba and G. F. Gribakin, Phys. Rev. A **49**, 2483 (1994); **50**, 3551 (1994).

[33] V. A. Dzuba, V. V. Flambaum, P. G. Silvestrov, and O. P. Sushkov, J. Phys. B **20**, 1399 (1987); Phys. Lett. A **131**, 461 (1988); V. A. Dzuba, V. V. Flambaum, and O. P. Sushkov, *ibid.* **140**, 493 (1989).

[34] S. A. Blundell, W. R. Johnson, and J. Sapirstein, Phys. Rev. A **38**, 4961 (1988).

[35] V. A. Dzuba, V. V. Flambaum, G. F. Gribakin, and W. A. King, Phys. Rev. A **52**, 4541 (1995).

[36] V. A. Dzuba, V. V. Flambaum, G. F. Gribakin, and W. A. King, J. Phys. B **29**, 3151 (1996).

[37] G. F. Gribakin and W. A. King, Can. J. Phys. **74**, 449 (1996).

[38] G. G. Ryzhikh and J. Mitroy, Phys. Rev. Lett. **79**, 4124 (1997).

[39] G. G. Ryzhikh and J. Mitroy, J. Phys. B **31**, L401 (1998); J. Mitroy and G. G. Ryzhikh, *ibid.* **32**, 1375 (1999).

[40] J. Mitroy, M. W. J. Bromley, and G. G. Ryzhikh, J. Phys. B **35**, R81 (2002).

[41] J. Mitroy, M. W. J. Bromley, and G. G. Ryzhikh, in *New Directions in Antimatter Chemistry and Physics* (Ref. [5]), pp. 199–221.

[42] A. B. Migdal, *Theory of Finite Fermi-Systems and Applications to Atomic Nuclei* (Interscience, New York, 1967).

[43] J. S. Bell and E. J. Squires, Phys. Rev. Lett. **3**, 96 (1959).

[44] L. D. Landau and E. M. Lifshitz, *Quantum Mechanics*, 3rd ed. (Pergamon, Oxford, 1977).

[45] For electrons this also means the absence of the contributions of the target exchange potential.

[46] RPA provides reliable values of atomic dipole polarizabilities, see, e.g., M. Ya. Amus'ya, N. A. Cherepkov, and S. G. Shapiro, Zh. Eksp. Teor. Fiz. **63**, 889 (1972); [Sov. Phys. JETP **36**, 468 (1973)]; D. Kolb, W. R. Johnson, and P. Shorer, Phys. Rev. A **26**, 19 (1982); W. R. Johnson, D. Kolb, and K.-N. Huang, At. Data Nucl. Data Tables **28**, 333 (1983).

[47] G. F. Gribakin, in *Photonic, Electronic and Atomic Collisions (XXII ICPEAC), Proceedings*, edited by J. Burgdorfer, J. Cohen, S. Datz, and C. Vane (Rinton Press, Princeton, 2002), pp. 353–364.

[48] P. A. Fraser, Adv. At. Mol. Phys. **4**, 63 (1968).

[49] M. Charlton and J. W. Humberston, *Positron Physics* (Cambridge University Press, Cambridge, England, 2001).

[50] This cross section is given by $\bar{\sigma}_{2\gamma} = \pi r_0^2 (c/v)$, where v is the electron-positron relative velocity, see, e.g., V. B. Berestetskii, E. M. Lifshitz, and L. P. Pitaevskii, *Quantum Electrodynamics* (Pergamon, Oxford, 1982). Annihilation into two gamma quanta is allowed only for the zero total spin of the pair, $S = 0$. For $S = 1$ they annihilate into three photons. The corresponding spin-averaged cross section is almost 400 times smaller: $\bar{\sigma}_{3\gamma} = [4(\pi^2 - 9)/3]\alpha r_0^2 (c/v)$, where $\alpha = e^2/\hbar c \approx 1/137$.

[51] G. F. Gribakin and J. Ludlow, Phys. Rev. Lett. **88**, 163202 (2002); J. Ludlow and G. F. Gribakin, Phys. Rev. A **66**, 064704 (2002).

[52] J. Sapirstein and W. R. Johnson, J. Phys. B **29**, 5213 (1996).

[53] C. de Boor, *A Practical Guide to Splines* (Springer, New York, 1978).

[54] M. Ya. Amusia and L. V. Chernysheva, *Computation of Atomic Processes. A Handbook for the ATOM Programs* (IOP Publishing, Bristol, 1997).

[55] I. Bray and A. T. Stelbovics, Comput. Phys. Commun. **85**, 1 (1995); I. Bray and D. V. Fursa, Phys. Rev. Lett. **76**, 2674 (1996).

[56] I. Bray and A. T. Stelbovics, Phys. Rev. A **48**, 4787 (1993).

[57] J. Mitroy and G. Ryzhikh, J. Phys. B **32**, 2831 (1999).

[58] G. F. Gribakin and J. Ludlow, J. Phys. B **35**, 339 (2002).

[59] C. Schwartz, Phys. Rev. **126**, 1015 (1962); *Methods in Computational Physics* (Academic, New York, 1962) Vol. 2, pp. 241–266.

[60] P. Van Reeth and J. W. Humberston, J. Phys. B **31**, L231 (1998).

[61] G. F. Gribakin, Phys. Rev. A **61**, 022720 (2000).

[62] G. G. Ryzhikh and J. Mitroy, J. Phys. B **33**, 2229 (2000).

[63] R. A. Ferrell, Rev. Mod. Phys. **28**, 308 (1956).

[64] J. Mitroy and B. Barbiellini, Phys. Rev. B **65**, 235103 (2002).

[65] This is true to the extent that we neglect the small difference between the true and HF electron densities, and that between $|\psi_\varepsilon(\mathbf{r})|^2$ and $\rho_p(\mathbf{r})$.

[66] J. Arponen and E. Pajanne, Ann. Phys. (N.Y.) **121**, 343 (1979); See also B. Barbiellini, M. J. Puska, T. Torsti, and R. M. Nieminen, Phys. Rev. B **51**, 7341 (1986).

[67] L. J. M. Dunlop and G. F. Gribakin (unpublished).

[68] J. Ludlow and G. F. Gribakin, Ph.D. thesis, Queen's University, Belfast, 2003.

[69] J. Ludlow and G. F. Gribakin (unpublished).

[70] D. A. Varshalovich, A. N. Moskalev, and V. K. Khersonskii, *Quantum Theory of Angular Momentum* (World Scientific, Singapore, 1988).